Plasma-driven Z-pinch X-ray loading and momentum coupling in meteorite and planetary materials

J O H N L. R E M O[1], M I C H A E L D. F U R N I S H[2] and R. J E F F E R Y L A W R E N C E[2]

[1]Departments of Astronomy and Earth and Planetary Sciences, Harvard University, Cambridge,
MA 02138, USA, and Harvard-Smithsonian Center for Astrophysics, Cambridge, MA 02138, USA
[2]Sandia National Laboratories, P.O. Box 5800, Albuquerque NM 87185-1195, USA
(mdfurni@sandia.gov)

Abstract. X-ray momentum coupling coefficients, C_M, were determined by measuring stress waveforms in planetary materials subjected to impulsive radiation loading from the Sandia National Laboratories Z-machine. Velocity interferometry (VISAR) diagnostics provided equation-of-state data. Targets were iron and stone meteorites, magnesium-rich olivine (dunite) solid and powder ($\sim$5–300 μm), and Si, Al, and Fe calibration targets. Samples were $\sim$1-mm thick and, except for Si, backed by LiF single-crystal windows. X-ray spectra combined thermal radiation (blackbody 170–237 eV) and line emissions from pinch materials (Cu, Ni, Al, or stainless steel). Target fluences of 0.4–1.7 kJ/cm^2 at intensities of 43–260 GW/cm^2 produced plasma pressures of 2.6–12.4 GPa. The short ($\sim$5 ns) drive pulses gave rise to attenuating stress waves in the samples. The attenuating wave impulse is constant, allowing accurate C_M measurements from rear-surface motion. C_M was $1.9 - 3.1 \times 10^{-5}$ s/m for stony meteorites, 2.7 and 0.5×10^{-5} s/m for solid and powdered dunite, $0.8 - 1.4 \times 10^{-5}$ s/m for iron meteorites, and 0.3, 1.8, and 2.7×10^{-5} s/m respectively for Si, Fe, and Al calibration targets. Results are consistent with geometric scaling from recent laser hohlraum measurements. CTH hydrocode modeling of X-ray coupling to porous silica corroborated experimental measurements and supported extrapolations to other materials. CTH-modeled C_M for porous materials was low and consistent with experimental results. Analytic modeling (BBAY) of X-ray radiation-induced momentum coupling to selected materials was also performed, often producing higher C_M values than experimental results. Reasons for the higher values include neglect of solid ejecta mechanisms, turbulent mixing of heterogeneous phases, variances in heats of melt/vaporization, sample inhomogeneities, wave interactions at the sample/window boundary, and finite sample/window sizes. The measurements validate application of C_M to (inhomogeneous) planetary materials from high-intensity soft X-ray radiation.

1. Introduction

This is an extension of previous works (Remo and Furnish 2002, 2008) describing high energy density (HED) experiments measuring soft X-ray coupling to a variety of materials on the Sandia National Laboratories (SNL) Z-pinch facility. The primary objective was to use soft X-rays to determine net momentum generation, pressure wave propagation, and momentum coupling coefficients, C_M, from mechanical responses to radiation on natural materials with astrophysical, planetary science, and near-Earth object (NEO) mitigation applications. Here, soft X-rays were produced with a spectrum peak of $\sim$12.5 Å. On-target radiation intensities varied from 43–260 GW/cm^2, with total fluences ranging from 0.3–1.7 kJ/cm^2. Targets included calibration metals (Fe and Al) and natural materials (iron and stony meteorites, and dunite). The inhomogeneous nature of meteorite

materials and dunite and their complex mechanical responses suggested that more homogeneous calibration materials be included to establish a basis of comparison.

In addition, a set of CTH hydrocode simulations of X-ray drive irradiation on silicate materials of various porosities was conducted allowing comparison with experimental C_M values and verification of the methodology for determining C_M. This provided insight into wave attenuation processes characterizing decreases in peak stress amplitude with position strongly influenced by porosity. Transmitted impulse remained constant with position in the target. Finally, an analytical deposition model (MBBAY) was applied to clarify trends and systematic behavior in material responses to X-rays. The present experiments were found to all lie at fluence levels well above those corresponding to the maximum values for C_M, the ratio of momentum to energy input.

A brief summary of the experimental phenomenology follows. Z-pinch radiation at $\sim$200 eV is formed by the collapse of a cylindrical wire array under the Lorentz forces produced by a $\sim$20-MA current pulse. This soft X-ray pulse (containing thermal and line components) irradiates sample surfaces. Diagnostic instrumentation characterizes fluence, time structure, and spectral properties of the X-ray pulse. At the sample surfaces energy is deposited, producing melt, vapor, and ejection materials. This leads to a sharply peaked stress wave, with a time duration of $\sim$3–8 ns, as well as a net impulse or momentum in the sample. The stress wave attenuates and broadens as it propagates due to dissipative compression processes such as hysteretic stress/strain loading loops, pore collapse, and phase transitions. Axial stress in the sample, σ_{zz}, varies over time and axial position, z. Momentum coupled to the sample at a given position, z, is given by the stress integral,

$$\frac{\text{Momentum}}{\text{Area}} = \int_0^{\infty} \sigma_{zz}(z,t)dt. \tag{1}$$

The observable is a velocity history, $v(t, z = \text{interface})$, at the interface between the sample and the LiF window. Converting this into σ_{zz} requires correcting for relative mechanical properties of the sample and the window (see Section 9) allowing momentum per area to be calculated via (1). Dividing this quantity by the integrated energy from the X-ray source gives C_M, which varies with material, X-ray intensity, and wavelength.

2. X-ray radiation source, absorption, and momentum coupling coefficients C_M

The Z-pinch hohlraum source radiation emission is composed of soft black-body (BB) and emission line components. The black-body spectrum corresponds to a temperature of $\sim$200 eV ($\sim$2,320,800 K) and (using the Wien displacement law or the Planck distribution) a peak radiation wavelength of $\sim$12.5 Å. From

$$\text{Energy} = \text{h}c/\lambda, \tag{2}$$

where h is Planck's constant and c is the speed of light, this corresponds to 1-keV photon energy. When derived in photon energy space (cf. Fig. 14), the peak is $\sim$0.6 keV. X-ray line emissions from the wire array material are somewhat harder (Ni: 8.3 keV, Al: 1.6 keV, Cu: 8.9 keV, or steel: 6.4 keV).

For X-ray absorption at energies $<$0.1 MeV, photoelectric cross-sections dominate and the Rosseland mean opacities, μ, may be used. For radiation of $\sim$200 eV, μ ranges from 170 to 1370 cm^2/gm. Taking an average target density, ρ, to be 3 g/cm^3, the soft X-ray penetration (skin) depth, $\delta = 1/(\mu\rho)$, varies from 2.4 to 20 µm. For 1-keV radiation from the peak of the 200-eV black-body source, μ varies from 170 to 10,000 cm^2/g, yielding a line penetration δ from 0.33 to 2.8 µm. Finally, the more energetic X-ray line emissions penetrate significantly deeper into targets than black-body radiation continuum. The relationship to ejecta

momentum (hence to C_M) is complex. More energy is required to vaporize a larger amount of material within a greater penetration depth, leaving less energy for material motion (jetting). X-ray ablation drive compression pressure in the subsonic deflagration regime may be expressed in the low drive limit (Atzeni and Meyer-ter-Vehn 2004) by

$$P_{\text{abl}} \approx P_{\text{Plasma}} = 2\rho c_t^2. \tag{3}$$

The corresponding intensity is

$$I_{\text{Rad}} = 4\rho c_t^3, \tag{4}$$

where P_{abl} is the ablation pressure, ρ is the plasma density, and c_t is the plasma isothermal speed of sound. For a stationary process $P_{\text{abl}} = P_{\text{plasma}}$.

C_M is measured in units of dyne-s/J or s/m $\times 10^{-5}$. Surface radiation-driven plasmas provide surface plasma pressure, P_{plasma}, from I_{Rad}, the incident radiation intensity,

$$C_M = P_{\text{plasma}}/I_{\text{Rad}} \approx 1/(2c_t). \tag{5a}$$

HED X-ray radiation interactions convert a portion of the target front surface into a high-pressure plasma, P_{plasma}, from I_{Rad} according to Lindl (1995),

$$P_{\text{plasma}}(\text{TPa}) = 17(\text{I}(\text{W}/(\text{cm}^2 \, 10^{15})))^{7/8}. \tag{6}$$

C_M is also expressed as momentum per unit area divided by front surface fluence, Φ_0,

$$C_M = (\text{momentum/area})/\Phi_0, \tag{5b}$$

where

$$\frac{\text{Momentum}}{\text{Area}} = \int_0^{\Delta} \rho_0 u_p(z)dz \tag{7}$$

In (7), momentum transfer is expressed over a distance interval, Δ. Momentum per unit area is now calculated from observed values and is equivalent to (1). Using (5a) and (6), $C_M \approx 10^{-5}$ s/m is in agreement with the impedance-corrected values for inhomogeneous targets listed in Table 5.

Stress history is measured by velocity history at VISAR, using the known compression curve of the LiF window, and by a correction, ψ, for re-shock/release reflected into the sample as discussed in Section 7. Momentum transfer/area over time interval t_1, substituting $dz = u_s dt$, with shock speed constant over dz, is

$$\frac{\text{Momentum}}{\text{Area}} = \int_0^{t_1} \rho_0 u_p u_s dt, \tag{8}$$

$$= \int_0^{t_1} P_{\text{window}} dt. \tag{9}$$

Integrating plasma pressure over the front surface energy (uniform) deposition over the plasma slab depth, δ, gives the radiative fluence, F_{Rad},

$$F_{\text{Rad}} = \int_0^{\delta} P_{\text{plasma}} dz \approx P_{\text{plasma}}\delta. \tag{10}$$

Although the functional form of $u_p(z)$ is not known within the target, u_p is measured (by VISAR) at the rear
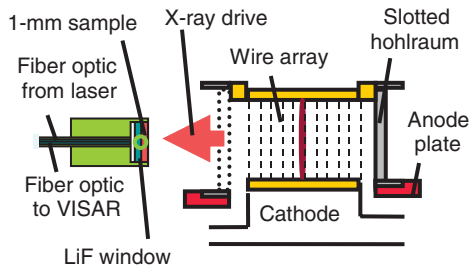
Figure 1. (Colour online) Experimental configuration. Wire array is cylindrical, with current through wires and returned through outer can (slotted hohlraum). (Reproduced from Remo and Furnish 2008 with permission from Elsevier.)

surface allowing an estimated pressure gradient, dP/dr, computation from the front to rear surface measuring energy dissipation within the target, equivalent to internal energy absorption. Assuming target and material invariance (5b),

$$\left[\int \rho_0 u_{\mathrm{p}}(z)dz\right] \Big/ \left[\int P_{\mathrm{plasma}}dz\right] = \frac{\rho_0 u_{\mathrm{p}}}{P_{\mathrm{plasma}}} = C_{\mathrm{M}}. \quad (11)$$

3. Experimental configuration

The experimental configuration in Fig. 1 (Remo and Furnish 2008) uses ~1-mm thick samples, backed by transparent (100) LiF crystals that allow in-material optical access to VISAR diagnostics. Without such a window, experience has shown that VISAR velocimetry would not be successful for many of these samples. Incident radiation generates pressures ranging from 2.6 to 12.4 GPa at surfaces exposed to Z-pinch radiation flux. These experiments were conducted under vacuum ($\sim 2 \times 10^{-5}$ torr).

Properties of the radiation pulse are shown in Fig. 2. The radiation pulse is of short duration (4–10 ns; see Fig. 2(b)). The resulting pressure pulse is narrow relative to the sample thickness, rapidly attenuating as it propagates through the sample. Attenuation rate depends on dissipative mechanisms within the sample, including pore crushing, phase transitions (solid/solid or melting), as well as plastic deformation.
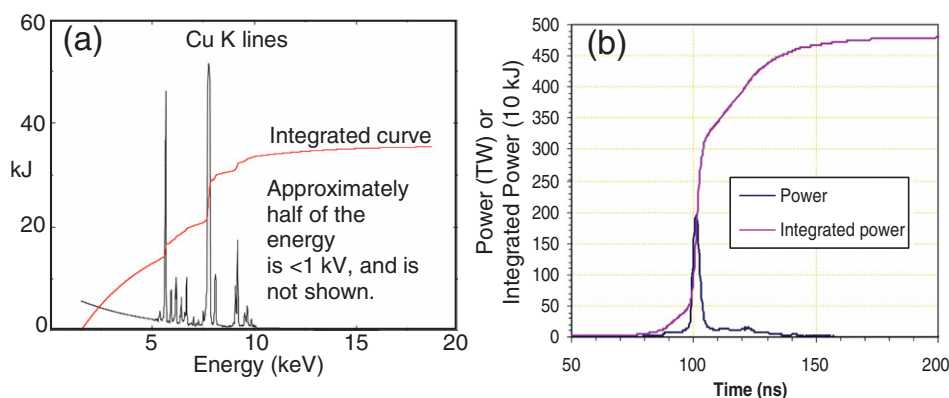
The targets were chosen to span a range of materials. In many cases it was possible to pair samples to allow comparisons of their behavior under identical drive conditions. This matrix is given in Table 1, together with radiation input parameters.

Natural materials' equation-of-state (EOS) determination is complicated due to their heterogeneous nature. VISAR diagnostics measure velocity at discrete points that are influenced by different phases of minerals within the sample, grain boundaries, and voids. Samples were not recovered, precluding post-irradiation microstructural analysis as were samples irradiated by high-intensity lasers (Remo et al. 2008).

4. Synthetic problem: radiation incident on silica

Inhomogeneities induce fluctuations in momentum density and particle velocity. Mineral phases with different densities force $u_{\mathrm{p}}, u_{\mathrm{s}}$, and P_{H} to fluctuate with energy absorption over time and distance, obscuring effects of energy loss and consequent wave attenuation effecting measurement of C_{M}. To illustrate the impact of wave attenuation on C_{M} measurement, synthetic problems utilizing the CTH (Hertel et al. 1993) wavecodes were constructed. In these simulations a 10-ns pulse of $0.8 \, \mathrm{kJ/cm^2}$ into solid silica (quartz, ~granite) is deposited in a zone of 4-μm thick. Radiation couples into the sample producing a stress wave of attenuating amplitude. Porous-sample pressure waves attenuate more rapidly due to work crushing pores. The loading wave is slowed relative to the overtaking rarefaction wave by large compressions leading to more rapid attenuation. Also, a recompression wave propagates back into the sample from the interface with the LiF window.

The GEO yield model was used (pressure-dependent yield surface), with a zero-pressure strength, Y_0, of 23 MPa, a limiting strength Y of 1.45 GPa, $(dY/dP)|_P = 0 = 0.846$, and Poisson's ratio, $v = 0.175$. Waveforms calculated for porosities of 0, 12, and 25% are shown in Fig 3.

Figure 2. (Colour online) Z-pinch radiation characteristics (a) Per-bin and integrated energy (case of copper wire array in shot Z636), courtesy B. Jones (2004, personal communication). Approximately half of the energy is Planckian radiation at <1 kV and is not shown. (Reprinted by permission from Remo et al. 2012, Copyright 2012, American Institute of Physics.) (b) Time structure of radiation from pinch (case of shot Z1747).

Table 1. Z-pinch shot matrix and conditions. Wire is the pinch material. E_z is the total shot energy. R is the distance from the center of the pinch, Φ_0 is the fluence at the sample, τ is the half-max pulse duration intensity at the surface of the target at distance R as given by the formula, $I_R = E_z/(4\pi R^2\tau)$ is the intensity at the target surface, T_{zpinch} is the effective black-body temperature at the plasma pinch hohlraum, and P_{plasma} is the calculated (Lindl) plasma pressure.

Shot # /Samples	Wire mat'l	E_z (kJ)	R (cm)	Φ_0 (kJ/cm^2)	τ (ns)	I_R (GW/cm^2)	T_{zpinch} (eV)	P_{plasma} (GPa)
636/Og^a, FeNi	Ni	1187	10	0.945	4.3	220	217	10.6
1184/Og^a, Fe	Al	880	7	1.429	7.4	193	176	9.5
1310/Al, CV3^a	Cu	1055	7	1.713	6.6	260	189	12.4
675/CV3^a mesosiderite	Cu	867	14	0.352	8.2	43	170	2.6
676/CV3^a refract. chondrite	Cu	1116	14	0.453	3.9	116	216	6.1
1709/silicon (free surface)	Steel	1083	14.5	0.410	6	68	195	3.9
1747/solid dunite powdered dunite	Steel	1190	14.5	0.450	3.0	150	237	7.7

^{a}Og is an octahedrite; CV3 is a refractory chondrite (see Section 9).
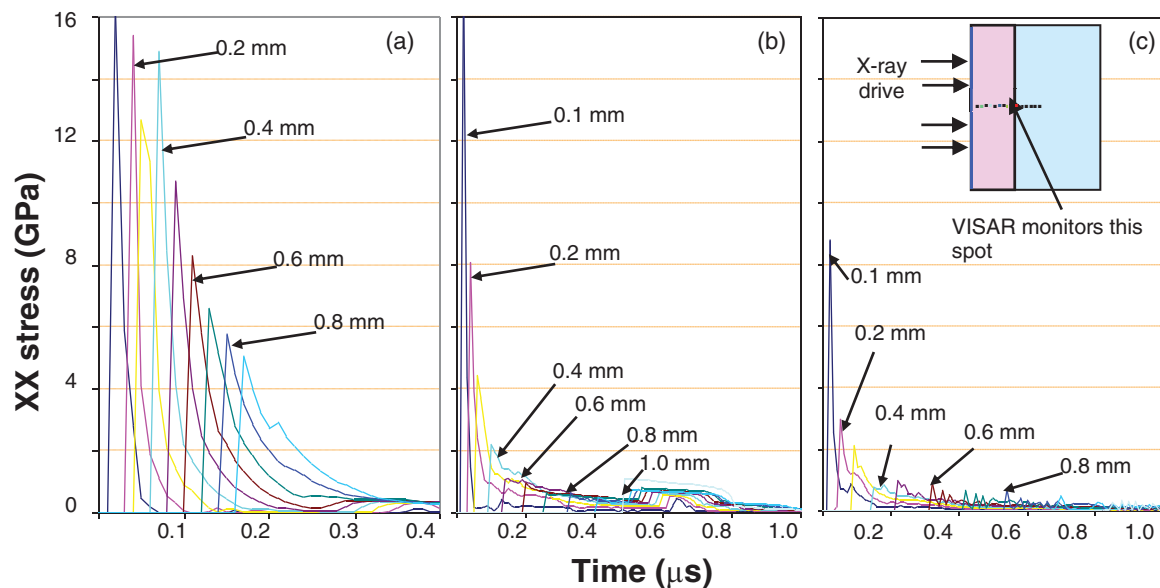

Figure 3. (Colour online) Calculations of pressure pulse (axial stress) with CTH from an X-ray energy deposition of 0.8 kJ/cm^2 in 10 ns to a 4-mm thickness of material on the left side. A LiF window is assumed. Pulse histories at tracer points initially at 0.1 mm are shown; selected histories are labeled. (a) Fully dense quartz sample, (b) 12% porous quartz sample, and (c) 25% porous quartz sample. (Reprinted by permission from Remo et al. 2012, Copyright 2012, American Institute of Physics.)

Impulses transmitted from plane to plane (outside the deposition zone) are constant during transit and independent of wave attenuation, although corrections are needed when waves pass from one material into another. These impulses are calculated using axial stress rather than pressure; the latter is complicated by material strength and potentially lateral confinement. Transmitted impulses for three cases as illustrated in Fig. 4 are based on time integration of pressure pulses calculated by CTH at selected Lagrangian positions.

For the case of fully dense silica (filled diamond symbols), the transmitted impulse is constant in the downstream 0.5 mm of the sample. The variations in the first 0.5 mm correspond to numerical imprecision in the representation of the relatively fast peaks, which were not adequately resolved by the recorded tracer history. This is less of an issue for the porous samples, in which the peaks are spread out over a larger span of time, even near the coupling region. However, for the 25% porous sample, time integrals of the axial stress for the
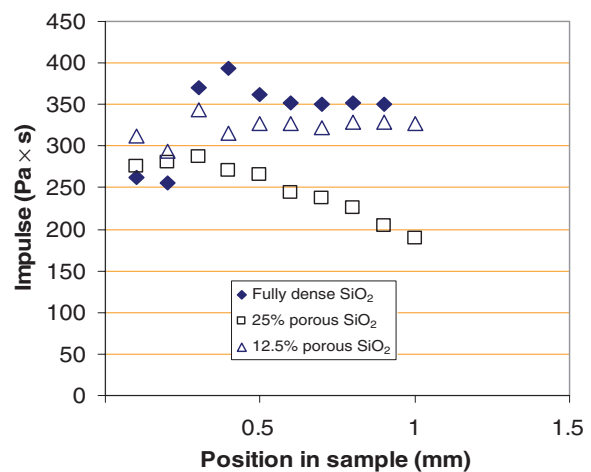

Figure 4. (Colour online) Impulse imposed at various depths within the sample for problems illustrated in Fig. 3 (fully dense polycrystalline quartz). Positions closer to the window interface (1 mm) are subject to error because of reflected reshock from the interface.
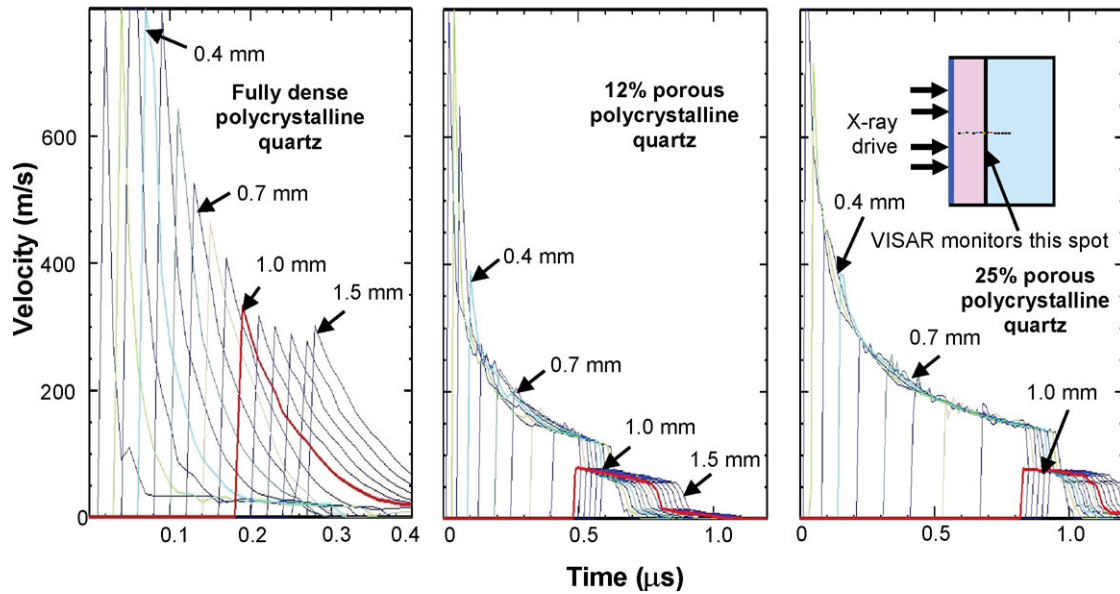
Figure 5. (Colour online) Calculations of material velocity histories with CTH for the problem of Fig. 3.
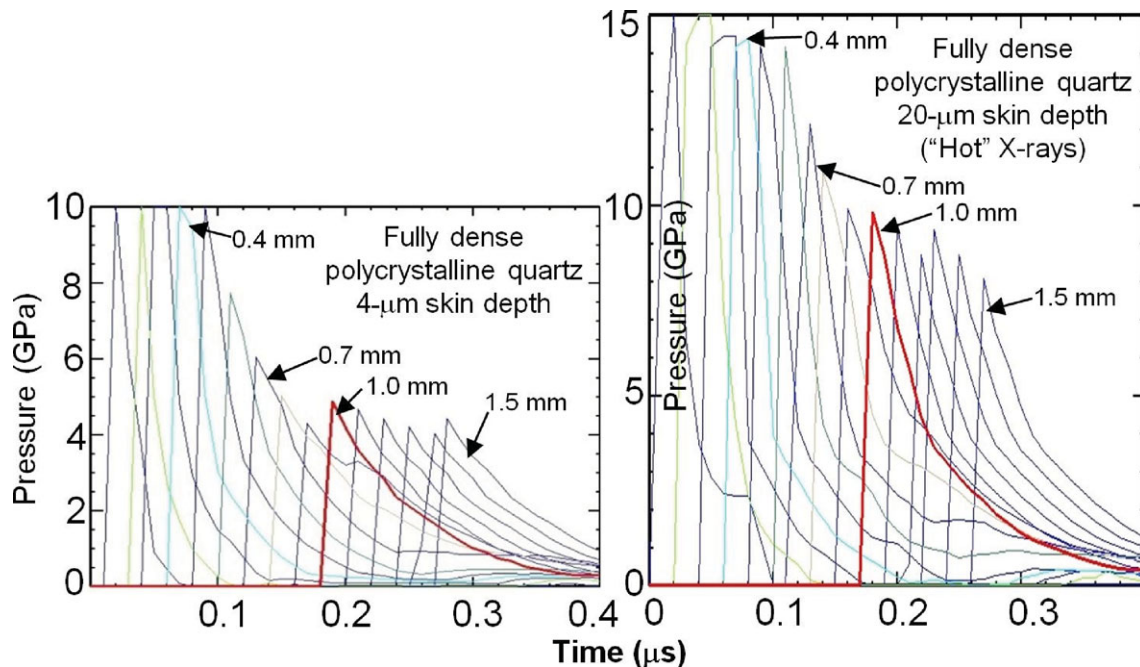

Figure 6. (Colour online) Comparison of loading wave in Fig. 3 problem (left-hand panel: X-ray energy deposition of 0.8 kJ/cm^2 in 10 ns to a 4-mm thickness of material on the left side) with similar problem where energy is deposited to a 20-mm thickness of material (right-hand panel).

tracer points progressively closer to the window/sample interface are affected progressively more at later times by wave interactions at this interface. This is exacerbated by the long tails to the pressure histories at each point in the sample. Wave evolution for these two cases may be related better to actual shot data if material (particle) velocities instead of axial stresses are plotted at various tracer points as shown in Fig. 5. Material velocities drop as the wave enters the LiF window reflecting higher shock impedance, $C_0\rho_0$, where C_0 is the bulk sound velocity of the window at zero wave amplitude. This

contrasts with the stress amplitude plot where stress levels increase as the wave enters the window.

It is also illustrative to hold the initial density constant (using a fully dense starting sample) and vary the energy deposition depth. A deposition depth of $\sim$20 μm (corresponding to more penetrating X-rays from a blackbody source at $\sim$1 keV) results in a larger impulse being transmitted into the sample from a correspondingly larger amount of ejecta (Fig. 6). For experiments on the Z-machine, X-ray skin depth ranges from < 1 micron (Fe target, < 1 keV X-rays) to the tenth of

Table 2. Elemental compositions of the meteorite materials used in the present study
(M. L. Petaev, 2010 personal communication).

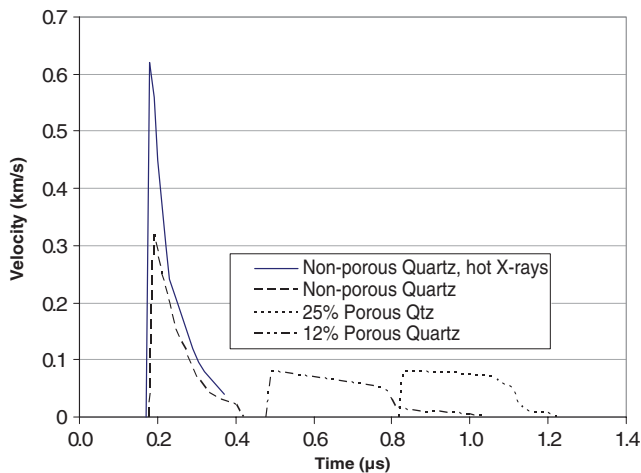| Rock (wt%)	Si	Al	Fe	Mg	Ca	Na	P	O	Ni	S
Dunite (terrestrial)	19.59	0.59	4.65	30.63	0.12	–	–	44.43	–	–
Barea mesosiderite	10.34	2.16	55.64	4.07	1.85	0.09	0.23	18.72	6.30	0.60
Vacamuerta mesosiderite	20.52	4.43	15.47	7.17	4.85	–	0.71	40.36	–	6.49
Allende (CV3) chondrite	17.02	1.84	22.65	15.80	1.98	0.35	–	38.79	–	1.56
Tuxtuac ((LL6) refr. chondr.	20.31	1.29	16.50	16.28	1.43	0.74	–	40.10	1.42	1.94
Odessa (Og) octahedrite	–	–	92.60	–	–	–	–	–	7.40	–

Figure 7. (Colour online) CTH simulation of quartz momentum uptake. Energy deposition region is 4-mm thick (20 mm for hot X-rays). Energy deposited is $0.8\,\text{kJ/cm}^2$, in 10 ns.

a millimeter (Fe or Cu line emission; silicate targets). These three synthetic problems yield velocity profiles in Fig. 7, emphasizing increased wave amplitude for the system with greater energy deposition depth, and decreased wave speed and greater velocity dispersion for a system with greater porosity.

5. Sample descriptions and loading states

Materials irradiated in this study include selected iron and stony meteorites, magnesium-rich olivine (dunite), and Al and Fe calibration materials. Compositions of the meteorites and dunite are given in Table 2 and Appendix A. Approximate Hugoniot values at the rear surface in Table 3 (Remo and Furnish 2008) are calculated from observed maximum particle velocity at the sample/window interface and mean wave speed. Particle velocity measurement was the dominant uncertainty, and is here reported corrected from the observed waveforms for impedance mismatch (see Section 6). Observed waveforms leading with these values are shown in Section 10.

Compared with the pure Fe target, the inhomogeneous octahedrite (Og) has a reduced rear-surface stress state because of absorption in interstices, inclusions, voids, and grain boundaries that generate variances in the Og as opposed to the uniform Armco calibration values. Results are consistent with a uniform radiation drive on the front surface. Dunite has higher bulk and shear moduli and is more homogeneous than the meteorites.

6. Impedance-matching corrections for C_M

When a loading wave passes from one material into another of different shock impedance, $C_0\rho_0$, a re-shock or release wave is reflected back into the sample and an impulse is transmitted into the second material (a window such as LiF). Since the observed data allowing calculation of an impulse is from the wave propagating into the window, we define a correction factor ψ multiplied by the observed impulse to give an *in-situ* sample impulse. For a fully dense quartz or aluminum sample, backed by a LiF window, ψ is near unity because the impedance mismatch is small. If the sample has a higher impedance than the window, a release propagates back into the sample and the momentum-coupling coefficient is underestimated, i.e. $\psi > 1$. This is illustrated in Fig. 8, which draws on "impedance match" methods of calculating dynamically loaded states (McQueen et al. 1970). For example, iron has an impedance of $C_0\rho_0 \approx 31.4 \times 10^6\,\text{kg/(m}^2 \cdot \text{s)}$ and a LiF window has an impedance of $C_0\rho_0 \approx 13.6 \times \cdot 10^6\,\text{kg/(m}^2 \cdot \text{s)}$, with C_0 in km/s and ρ_0 in g/cm^3, giving an underestimate of C_M by $\sim 2\times$ and making it necessary to multiply the derived C_M by

$$\psi = (M_1 + M_2)/(2M_2), \qquad (12)$$

correcting this effect. M_1 is $C_0\rho_0$ for the sample and M_2 is $C_0\rho_0$ for the window. Correction factors, ψ, together with pressure versus particle velocity slopes, M, are given in Table 4.

7. Observed waveforms and derived momentum coupling

Although introduction of energy (and momentum) into the samples occurs over a timespan of 3–8 ns, the properties of different samples give rise to different waveforms at the sample/window interface. In general, more porous samples exhibit more dispersive properties giving a slower waveform rise and longer pulse duration, thereby imparting a smaller target acceleration. A key point of this analysis is to integrate the pressure pulse over the entire pulse duration to derive the actual total momentum uptake of the particular sample, depending on whether the target is solid, porous, or powder. It

Table 3. Z-pinch shock loading (Hugoniot) parameters for rear surfaces of meteorite and calibration targets, with reference values. The target thickness is labeled as d. Results for two spots on one target are shown as separate lines.

Shot	d (mm)	ρ_0 (kg/m^3)	ρ (kg/m^3)	U_P (km/s)	U_S (km/s)	P_H (GPa)
			Allende CV3 chondrite			
675	1.012	2910	2925	0.030	5.70	0.498
676	1.014	2910	2967	0.025	5.73	0.424
1310	1.000	2910	2922	0.098	3.73	1.07
			Vacamuerta mesosiderite			
675	1.013	3600	3634	0.035	3.78	0.48
			Tuxtuac refractory chondrite			
676	1.010	3020	3052	0.059	5.71	1.10
			Dunite			
1747	0.994	3300	3342	0.065	5.212	1.12
Ref. value[a]		3300	3319	0.090	6.80	2.03
			Powdered dunite			
1747	1.284	2640	2709	0.071	2.79	0.53
			Odessa/Og (iron/nickel)			
636	1.508	7210	7270	0.035	4.16	1.04
1184	1.0	7210	7290	0.049	4.44	1.56
			Armco Fe			
1184	0.9	7850	7990	0.085	4.85	3.23
Ref. value[a]	–	7850	7856	0.140	4.65	5.11
			Al 2020			
1310	1.0	2703	2990	0.600	6.25	10.14
Ref. value[b]	–	2703	2784	0.610	6.16	10.5
			Silicon			
1709	1.207	3300	3389	0.320	12.23	12.91

[a]Hicks et al. (2010), p. 380 (interpolated in U_P between zero pressure and the lowest dynamic point).
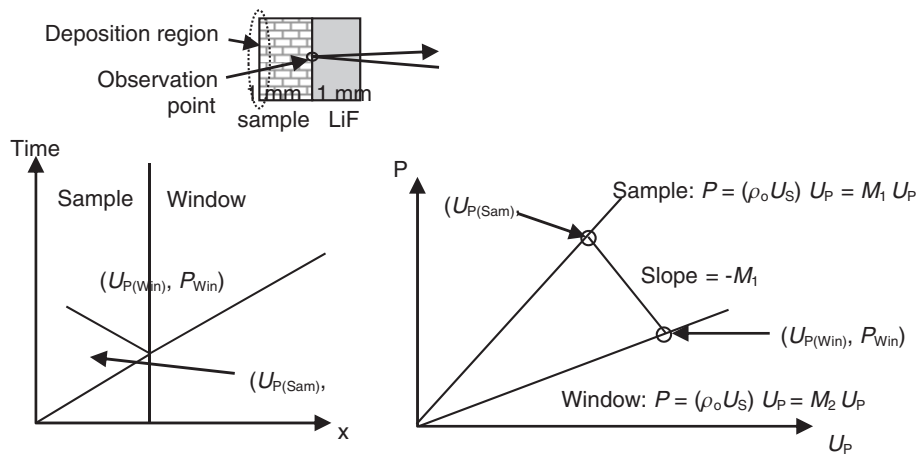[b]Hicks et al. (2010), p. 166 (based on U_S/U_P fit for 2024 Al).

Figure 8. Illustrative correction to C_M required by the use of a window such as LiF where stress levels in the window are lower than in the sample if the window has a lower shock impedance, $\rho_o U_S$, than the sample.

will also vary with the radiation cross section with possible scabbing of a layer of material, heat of vaporization, and other properties. If there is no spallation, as in the present experiments where samples are backed (confined) by a window, net momentum transfer to the target depends only on front (initial) surface ejecta via conservation of momentum.

The finite size of the LiF windows imposes limits on the time interval in which the observed waveform is useful. When wave propagation is highly dispersive (resulting in loading and release wave spread), the leading portion of the wave may reach the back of the LiF window before the entire wave has reached the sample/LiF interface. In this case, motion $v_s(t)$ of the LiF free surface must be considered. Dolan (2006) shows that the actual velocity $v(t)$ of the reflecting surface is related to the apparent velocity $v^*(t)$ as:

$$v(t) = (1/a)[v^*(t) + (a - 1)v_s(t)], \qquad (13)$$

where a, the velocity correction due to the dynamic index of refraction, is 1.280 for LiF at 532-nm light. Since we did not explicitly measure $v_s(t)$, it must be approximated. For the first 189 ns after the sample/LiF interface moves, $v_s(t)$ will be zero because the wave

Table 4. C_M correction factors ψ for different samples with LiF windows. The value of $M_1 = 13.6 \times 10^6$ kg/(m$^2 \cdot$ s) for LiF is also M_2 for the LiF windows for all samples. The Si sample is not included because that test did not use a LiF window.

Sample	$M_1 10^6$ kg/(m$^2 \cdot$ s)	ψ
LiF	13.6	1.0
Iron	31.4	1.65
Chondrite	16.3	1.1
Mesosiderite	16.3	1.1
Refractory chondrite	16.3	1.1
Aluminum	14.3	1.025
Solid dunite	22.1	1.31
Powdered dunite	7.32	0.77
Z-Quartz (CTH)	17.0	1.12
12% porous quartz	4.3	0.66
25% porous quartz	3.2	0.62

(propagating $\sim$5.6 km/s) has not had time to traverse the 1-mm thick LiF. Following this time a 0th order approximation that $v_s(t) = 2v(t - 189\,\text{ns})$ is used, i.e. the wave is transmitted unmodified through the LiF. However, when the loading wave propagating through the window has had time to reflect from the back of the window and arrive again at the sample interface, the actual motion of the interface is affected. This occurs at a time (2 mm)/(5.3 mm/µs) = 377 ns after initial motion. Data are disregarded after this time.

Waveforms from chondrite and 1100 aluminum, acquired on test Z1310, are shown in Fig. 9. The aluminum waveform, with rapid loading and immediate pullback, indicates a classic attenuating wave. By contrast, the (polyphase) chondrite waveform is dispersed and irregular. Intervals of integration are indicated by shading (for the chondrite) and a dotted cutoff line (for the aluminum).

Octahedrite, composed of iron–nickel domains of kamacite and taenite, and Armco iron samples on shot Z1184, show dispersed loading followed by a pullback (Fig. 10). Armco iron shows approximately twice the amplitude of the octahedrite, a surprise in view of the similar densities and X-ray stopping powers of both materials. Like Z1310, natural samples with micro inclusions and grain boundaries show more irregular waveforms, energy absorption, and compression wave speed reduction than uniform samples.

Shot Z1747 used monolithic and powdered/compressed dunite targets. Porous targets indicated a decrease in compression wave speed analogous to the synthetic problems discussed in Section 5 (cf. Fig. 7). Waveforms for monolithic dunite (Fig. 11), exhibiting two sharp separate peaks, suggest yielding phenomenon.

Waveforms from other samples are shown in Fig. 12. The waveform for the octahedrite (Z636) is similar to Fig. 9, except for a second peak. Timing of the second peak suggests an expansion wave corresponding to a reflection from the back of the LiF window and is discounted. Similar features are shown for chondrite and mesosiderite (Z675), and are also discounted. Waveforms for the refractory chondrite shot Z676 also shows this feature but do not cleanly indicate where the reflected shock effect begins.

Finally, a waveform was obtained for polycrystalline silicon. For this sample no window was used, and the rear surface was therefore a free surface. The waveform, shown in Fig. 13, shows a much less dispersed wave than other samples. This is probably due to the higher wave speed of Si ($\sim$9 km/s), both for loading and release, as well as the high strength, causing most of the wave behavior to be elastic.

Calculation of C_M proceeds by integrating the velocity curve over the time curve in the window with its bounds, and converting it into a pressure–impulse using the approximate relation for LiF, which is $P = (\rho_0 \cdot U_S) \cdot U_P \approx 13.59$ GPa, where U_P is the observed
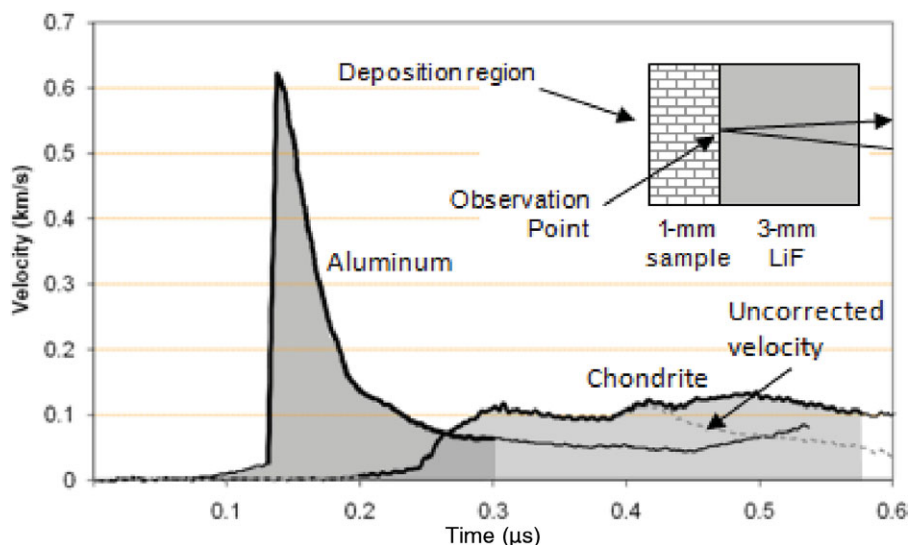

Figure 9. (Colour online) Experimental result for momentum uptake in 1100 Al and chondrite. Energy deposited is 1.73 kJ/cm^2, deposited in $\sim$5 ns FWHM (experiment Z1310). Integration intervals are indicated. (Reprinted by permission from Remo et al. 2012, Copyright 2012, American Institute of Physics.)
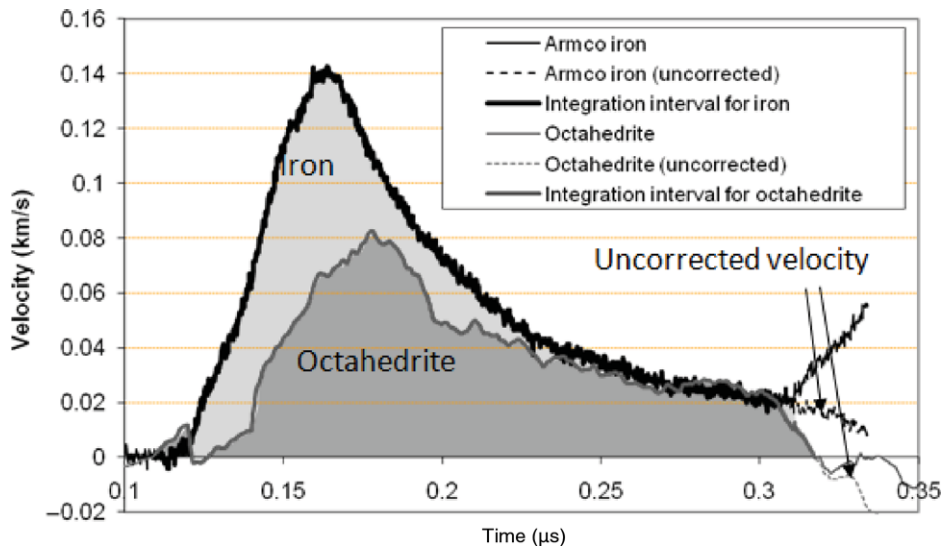
Figure 10. (Colour online) Experimental results for momentum uptake in Armco iron and an octahedrite sample. Energy deposited is $1.43 \, \text{kJ/cm}^2$, deposited in ~ 5 ns FWHM (experiment Z1184). The below-zero portion at late time is an artifact of the effect of the loading wave arriving at the rear surface of the LiF window.
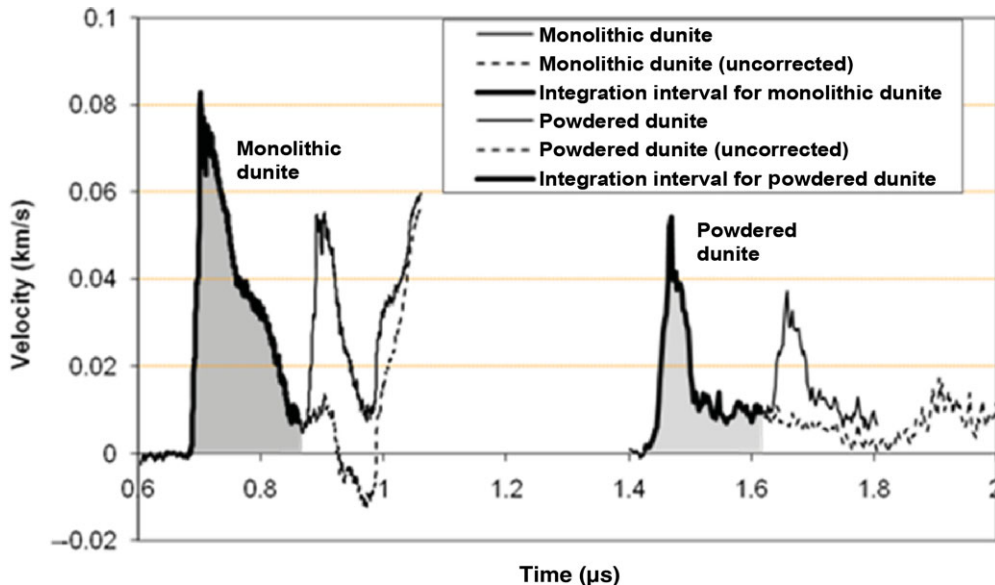

Figure 11. (Colour online) Experimental results are shown for momentum uptake in dunite $((\text{Mg}_{0.9}\text{Fe}_{0.1})_2\text{SiO}_4)$, both monolithic and powdered/compressed. Energy deposited is $0.45 \, \text{kJ/cm}^2$, deposited in ~ 5 ns FWHM. Powdered dunite has a lower wave speed than solid dunite, resulting in a later waveform arrival (experiment Z1747).

velocity in the window. This value is corrected for impedance mismatch between samples and windows by applying Table 2 correction factors. Corrected values for impedance matching C_M are determined from

$$C_M = (\text{momentum/area})/\Phi_0 \times \psi, \quad (14)$$

$$C_M = \left[\int_0^{t_1} \rho_0 U_P U_S \, dt \right] / \Phi_0 \times \psi. \quad (15)$$

Corrected C_M values are listed in Table 5, agreeing with earlier results (Shafer et al. 1994, 1997). Low C_M values for powdered samples are due to low velocity transfers. If energy density decreases below an ejection threshold, C_M decreases markedly.

7.1. Observed waveforms – Recent corroborating work

A recent laser-driven hohlraum plasma implosion experiment (Hicks et al. 2010) on Cu-doped Be targets corroborates the present results. On the Omega laser facility, a vacuum hohlraum of radius $r = 0.8$ mm was created at a temperature, $T = 200$ eV and pressure, $P \sim 10^{13}$ Pa. Measurements of the implosion of the initially 0.42-mm (outer diameter) target may be used to estimate a momentum coupling coefficient as

$$C_{M\,\text{Hohlraum}} = P/I = 0.62 \times 10^{-5} \, \text{s/m}, \quad (16)$$

where the hohlraum black-body intensity, $I = 160 \, \text{TW/cm}^2$, is calculated from the 200-eV hohlraum temperature.
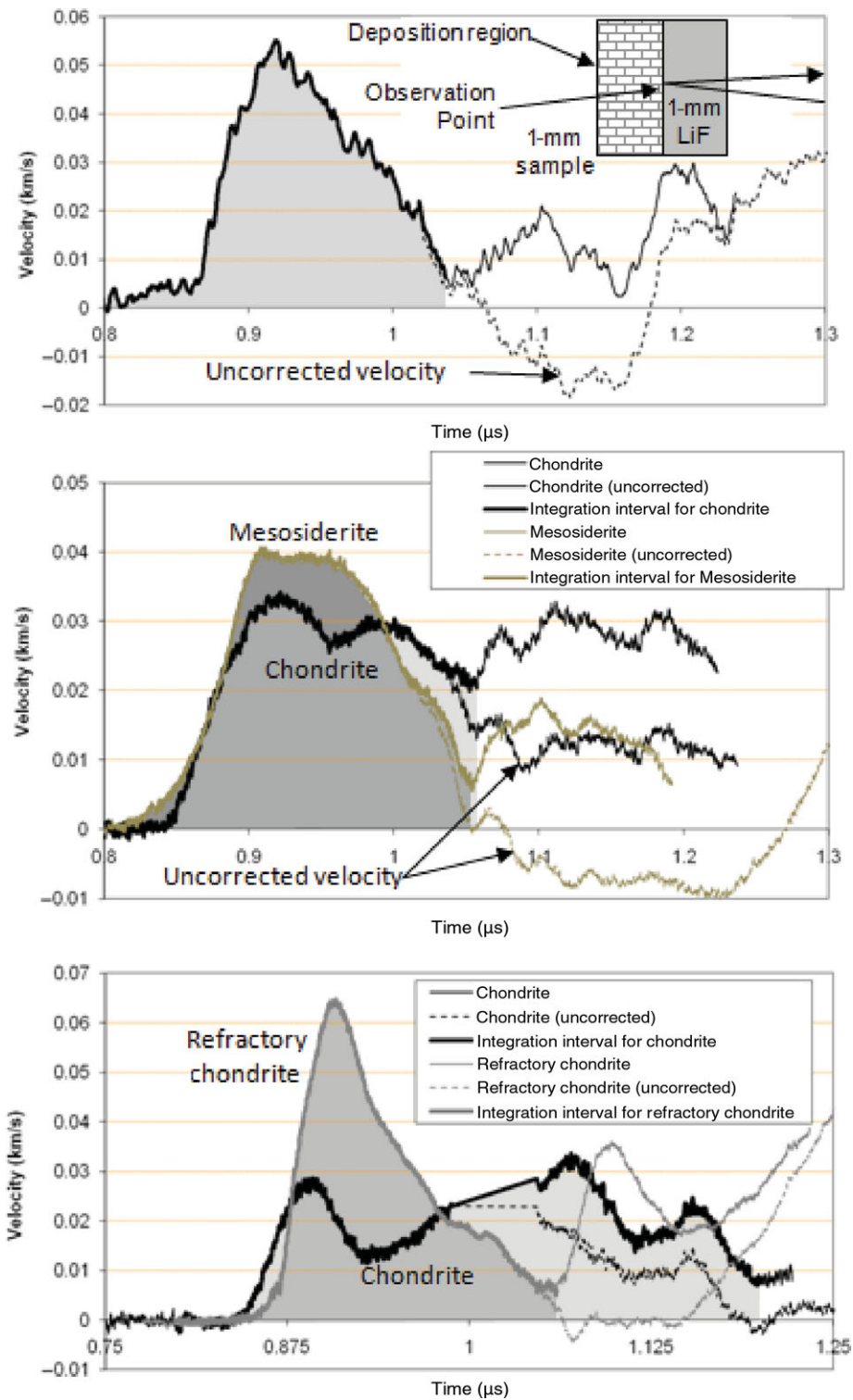
Figure 12. (Colour online) Experimental results for momentum uptake in (a) an octahedrite ($0.945\,\text{kJ/cm}^2$; experiment Z636), (b) a chondrite and a mesosiderite ($0.352\,\text{kJ/cm}^2$; experiment Z675), and (c) a chondrite and a refractory chondrite ($0.453\,\text{kJ/cm}^2$; experiment Z676) are shown. Shaded areas indicate integration intervals for C_{M}.

It is interesting to ask what this result would predict for the same target (Cu-doped Be) at a radius, $R = 7\,\text{cm}$. Recalling (5a), we calculate the isothermal sound speed in the plasma medium as

$$c_{\text{t}} = [K_B T/(A\,m_p/(Z + 1))]^{1/2}, \qquad (17)$$

where m_p is the proton mass, K_B is the Boltzmann constant, A is the atomic number, and Z is the ionization level. Referring to (5a),

$$C_{\text{M}} = 1/(2c_{\text{t}}) = \tfrac{1}{2}[K_B T/(A\,m_p/(Z + 1))]^{-1/2}. \qquad (18)$$

Table 5. C_M calculation from impulse integration using (10) and (14). The plasma pressure is generated on the target front surface by the Z-pinch radiation. Note, the quotient of the pressure divided by the fluence must be multiplied by the correction factor ψ to obtain C_M (see (6) and (9)).

| Shot #	Sample	ρ_0 (gm/cm^3)	Fluence (J/cm^2)	$\int v dt$ (μm)	$\int P dt$ (kPa·s)	ψ (Table 4)	C_M (10^{-5} s/m)	P_{Plasma} (GPa)
636	Octahedrite	7.21	945	5.97	0.0811	1.65	1.42	10.7
675	Mesosiderite	3.60	352	5.70	0.0774	1.1	2.42	2.6
675	CV3 allende	2.91	352	5.30	0.0721	1.1	2.25	2.6
676	Refr chondr.	3.02	453	5.66	0.0769	1.1	1.87	6.1
676	CV3 allende	2.91	453	7.18	0.0976	1.1	2.37	6.1
1184	Octahedrite	7.21	1429	5.24	0.0712	1.65	0.82	9.6
1184	Armco Fe	7.85	1429	11.12	0.1512	1.65	1.75	9.6
1310	CV3 allende	2.91	1713	35.70	0.4851	1.1	3.12	12.4
1310	Al 2100	2.70	1713	32.54	0.4423	1.025	2.65	12.4
1709	Silicon (free surf)	2.33	410	1.13	0.0118	2.0	0.29	3.9
1747	Dunite	3.30	450	6.75	0.0907	1.31	2.67	7.7
1747	Pwd dunite	2.64	450	3.08	0.0419	0.9	0.49	7.7
CTH	Quartz	2.64	800	22.46	0.3052	1.12	4.27	8.1
CTH	12% porous quartz	2.32	800	22.41	0.3046	0.66	2.51	8.1
CTH	25% porous quartz	2.00	800	22.55	0.3065	0.62	2.38	8.1
CTH	Quartz (hot X-rays)	2.64	800	42.78	0.5813	1.12	8.14	8.1?
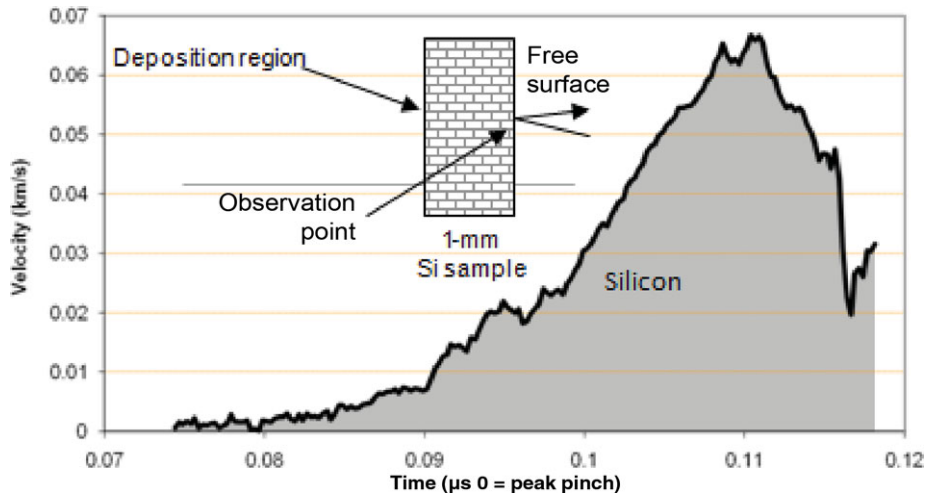
Figure 13. (Colour online) Experimental results for momentum uptake in polycrystalline silicon (0.410 kJ/cm^2; experiment Z1709). The shaded area indicates integration intervals for C_M.

We now have the scaling relationships, $c_t \sim T^{1/2}$ and $c_t \sim I^{1/8}$, and $C_M \sim T^{-1/2}$ and $C_M \sim I^{-1/8}$. Note that $R \gg r$, so the target is external to the hohlraum. The scaling factors are used to determine the momentum coupling coefficient within the hohlraum at radius r,

$$C_{M\,Hohlraum}$$
$$= [(Z_H + 1)/(Z_T + 1]^{-1/2} [I_H/I_T]^{-1/8} C_{M\,Target}. \quad (19)$$

We assume that $Z_H \approx Z_T$; i.e. the ionizations are about the same at the hohlraum and target intensities. Therefore,

$$C_{M\,Hohlraum} = [T_H/T_T]^{-1/2} C_{M\,Target} = [r/R]^{1/4} C_{M\,Target}, \quad (20)$$

where T_H and T_T are the hohlraum and target temperatures respectively, and the inverse square dependence

of intensity on radius is used. Since $r = 0.8$ mm and $R = 7$ cm,

$$C_{M\,Target} = 0.33\,, \quad C_{M\,Hohlraum} = 1.9 \times 10^{-5}\,\text{s/m}. \quad (21)$$

This value is very close to our experimental values for metallic Armco iron and Al from Table 5 (1.75×10^{-5} s/m and 2.65×10^{-5} s/m respectively). Inclusion of the ionization-level corrections will only decrease $C_{M\,Hohlraum}$ by a few percent. This close agreement supports the reliability of both our experimental results and the physical model for soft X-ray radiation transport.

8. Analytic impulse models (MBBAY calculations)

An analytic model is used to investigate blowoff impulse and late-time momenta without dealing with a multi-dimensional hydrocode analyses is the so-called modified

BBAY (MBBAY) model by Bethe, Bade, Averell, and Yos in the 1960s and modified by McCloskey and Thompson in the 1970s (Newlander et al. 1978). Originally developed to study nuclear weapon effects, more recently it has been used to examine the interaction of nuclear explosions with comets or asteroids that might be on a trajectory with a high probability for impact with Earth (Hammerling and Remo 1995). The MBBAY model predicts the impulse, I, as

$$I = \alpha\sqrt{2}\left[\int_0^{z_0}\left\{E(z) - E_0\left(1 + \ln\frac{E(z)}{E_0}\right)\right\}\rho^2 z\,dz\right]^{1/2},$$

(22)

where $1 \leqslant \alpha \leqslant \sqrt{2}$, generally taken as $\alpha = 1.2$. $E(z)$ is the energy deposition per unit mass as a function of depth, z, in the target, and E_0 is the specific energy defining the extent of the material contributing to the blowoff impulse (i.e. where $E(z_0) = E_0$), and ρ is the target material density. E_0 is the target melt or vaporization energy. Integration is from the front surface, $z = 0$, to the blowoff depth, $z = z_0$. If the energy-dependent absorption coefficients, $\mu(h\nu)$, can be approximated by a single *effective* value, μ_{eff}, then the energy deposition, $E(z)$, can be expressed as

$$E(z) = \mu_{\text{eff}}\Phi_0 \exp(-\mu_{\text{eff}}\rho z),$$

(23)

where Φ_0 is the incident energy fluence. The MBBAY model is integrated to yield a relatively simple closed-form expression for the impulse. Representing the impulse in a non-dimensional form, $I^* = \mu_{\text{eff}}I/E_0^{1/2}$, as a function of the non-dimensional fluence, $\Phi_0^* = \mu_{\text{eff}}\Phi_0/E_0$; following Lawrence (1992), the result is

$$I^* = \alpha\sqrt{2}\left\{\Phi_0^* - \left[1 + \ln\Phi_0^* + \frac{1}{2}(\ln\Phi_0^*)^2\right.\right.$$
$$\left.\left. + \frac{1}{6}(\ln\Phi_0^*)^3\right]\right\}^{1/2}.$$

(24)

In the limit of high fluence, $\Phi_0^* \gg 1$ the logarithmic terms in the square brackets increase more slowly than the other terms, and the equation reduces to

$$I^* = \alpha\sqrt{2\,\Phi_0^*}, \quad \Phi_0^* \gg 1.$$

(25)

Changing back to dimensional variables, this becomes

$$I = \alpha\sqrt{\frac{2\Phi_0}{\mu_{\text{eff}}}}, \quad \Phi_0 \gg E_0/\mu_{\text{eff}},$$

(26)

and at high fluences the impulse is asymptotically independent of all material properties but the absorption coefficient, and scales with the square-root of the incident fluence.

There are three important properties of this model that apply for the approximate forms described above or for full numerical integrations over depth into the target and over spectral intensities and absorption coefficients. First, there is a deposited energy, below which there is no material decomposition and thus no generated

blowoff impulse. This assumes that deposited energy is a monotonic decreasing function of the depth in the target as suggested above. For a given X-ray spectrum and target material this leads to a specific threshold for the incident energy fluence located at $\Phi_0^* = 1$. Second, if the impulse coupling coefficient, C_M, is defined as the impulse, I, divided by the energy fluence incident on the surface of the target, Φ_0, then C_M will have a maximum value at a fluence roughly by a factor of 10 greater than the threshold, i.e. at $\Phi_0^* \approx 10$. Finally, when the incident fluence is high – much greater than at the maximum coupling efficiency or the knee of the impulse curve – the impulse will scale with the square-root of the incident fluence, as shown above. For fluences at higher levels, the impulse will be relatively insensitive both to the characteristics of the incident radiation, other than its absorption coefficient in target materials, and to other target properties. For applications depending on impulse coupling, it may be important to choose, if possible, an incident X-ray spectrum that maximizes this coupling and/or its efficiency.

9. X-ray spectra and blowoff impulse

To calculate the blowoff impulse in the solid materials, a description of the X-ray spectra generated by the wire arrays constituting the magnetically driven Z-pinch is necessary, including both X-ray spectra and fluences incident on target materials. Relevant fluences, as well as the *measured* impulses and coupling coefficients, are provided in Table 5 and excerpted in Table 6. Each of the wire array materials has its own line spectrum constituting approximately 5% of the fluence incident on the target. The bulk of the fluence – the remaining 95% – is thermal in nature, and is approximated as a blackbody or Planckian spectrum with a nominal temperature of 200 eV (1 eV = 11,604 K). Note that the peak intensity for this thermal spectrum occurs at a photon energy of 0.56 keV (i.e. 2.82 times the temperature), and that 99% of its total energy is at photon energies below 2 keV (i.e. 10 times the temperature). The appropriately weighted line and thermal components of the spectrum are then summed to provide the source term for the target response. The process is illustrated using the copper-wire-array spectrum, which constitutes half of the shots examined. Figure 14 and its caption show the results. A similar process is repeated for the nickel, aluminum, and stainless steel wire arrays.

Target material properties are listed in Table 7. To calculate the energy deposition, the inputs required by the X-ray deposition code (Lowen et al. 1993) include the X-ray spectrum, the target composition, and the target densities, ρ_0. Photoelectric absorption is dominant, but Compton scattering and emission of fluorescence radiation are also fully taken into account. Since energy deposition processes are all on an atomic basis, errors associated with this aspect of analysis are very small.

Table 6. Radiation environment and impulse data for samples. The shots with numbers followed by "a" and "b" contained two samples each – a meteorite material and a metal. The fluences are taken from Table 1. The MBBAY impulses and coupling coefficients were calculated using the MBBAY model as incorporated in the X-ray deposition code (Schafer et al. 1997). The numbers before the slash employed the standard values for the decomposition energies, and the numbers after the slash used element-weighted values based on the constituent elements. The measured impulses and coupling coefficients were obtained from integrated particle velocity records, and were taken from Table 5. The measured coupling coefficients do not follow directly from the impulses and fluences but were obtained using the impedance-matching method. Calculated and measured results show differences that may be due to approximations used in the MBBAY model or in data reduction techniques; inhomogeneities in samples could also be an important contributing factor. One standard unit of impulse, dyne-s/cm^2, is often called a "tap," where 1 tap = 0.1 Pa-s. Coupling-coefficient units are $(dyne - s/cm^2)/(J/cm^2) = $ dyne-s/J, where 1 s/m = 10^5 dyne-s/J.

| Shot number	Wire array material	Target material	Fluence on target (kJ/cm^2)	MBBAY impulse (Pa-s)	MBBAY coupling coefficient (10^{-5} s/m)	Measured impulse (Pa-s)	Measured coupling coefficient (10^{-5} s/m)
636	Nickel	Odessa	0.945	410/360	4.3/3.8	81	1.4
675	Copper	Allende	0.352	190/170	5.4/4.8	72	2.6
676	Copper	Allende	0.453	220/200	4.8/4.4	98	2.4
1184 a	Aluminum	Odessa	1.43	390/380	2.73/2.66	71	0.82
1184 b	Aluminum	Iron	1.43	390	2.7	150	1.8
1310 a	Copper	Allende	1.71	440/420	2.6/2.5	490	3.1
1310 b	Copper	Aluminum	1.71	700	4.1	440	2.7
1747	Stainless steel	Dunite (ALM-2)	0.450	240/220	5.3/4. 9	91	2.7
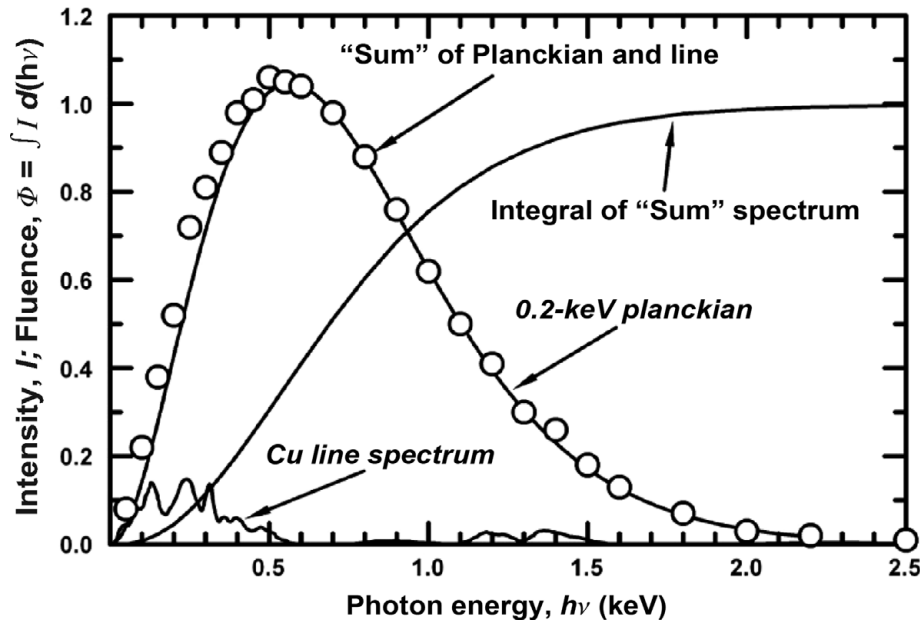
Figure 14. Source spectra for copper wire array. The curve labeled "0.2-keV Planckian" represents the thermal component of the fluence incident on the target, and is normalized to an integral of $\Phi = 0.95$. The "Cu Line Spectrum," normalized to $\Phi = 0.05$, shows the spectrum directly from the copper material constituting the wire array; it is a low-pass filtered version of the detailed experimental measurements. The circular points near the blackbody curve provide a numerical sum of two source spectra; they are the data actually used in the X-ray deposition code. Labeled "Integral of 'Sum' Spectrum," the final curve is the numerical integral of those latter points, and has a final value of $\Phi_{tot} = 0.999$. In the X-ray deposition code, this final "sum" spectrum is scaled to the desired fluence. Similar plots for each of the wire-array materials were also generated. (Reprinted by permission from Lawrence et al. 2012, copyright 2012, American Institute of Physics.)

However, the target materials are inhomogeneous on a sub-millimeter scale, so on this spatial dimension the locally deposited energy may have significant uncertainties. Averaged over the "homogenized" samples, this error is several percent. In addition, the MBBAY code requires the target melt, E_m, and vaporization, E_v, energies to calculate blowoff. The decomposition energies used for target materials are an additional source of uncertainty in these calculations.

Table 7 includes two sets of values for E_v and E_m, first for the standard values generally accepted for meteorite materials by the community, and second derived here to indicate potential uncertainties in the calculated impulse from this source. For the first values E_m, is assumed to be $\sim 0.1 E_v$, as is roughly the case for many elements. For the second values both E_v and E_m are calculated from the better-known properties of constituent elements using the elemental weight percentages given in

Table 7. Properties of target materials. Values of the vaporization (E_v) and melt (E_v) energies for the meteor materials are approximate and "homogenized" over the variable and inhomogeneous minerals. The values for E_v and E_m listed before the slash are those generally accepted by the community, with the latter approximated by $E_v/10$. The values after the slash are weighted by the elemental weight composition from the constituent elements. The elemental compositions may not add to 100 due to rounding.

Material	ρ_0 (g/cm^3)	E_v (kJ/g)	E_m (kJ/g)	Elemental weight percentage									
				O Z = 8	Na Z = 11	Mg Z = 12	Al Z = 13	Si Z = 14	S Z = 16	Ca Z = 20	Cr Z = 24	Fe Z = 26	Ni Z = 28
Allende	2.91	6.0/12.0	0.6/2.5	39	0.4	16	1.8	17	1.6	2.0	–	23	–
Dunite (ALM-2)	3.3	6.0/13.0	0.6/1.9	44	–	31	0.6	20	–	0.1	0.3	4.6	–
Odessa	7.21	6.4/7.4	0.64/1.3	–	–	–	–	–	–	–	–	93	7.4
Aluminum	2.7	13.5	1.05	–	–	–	100	–	–	–	–	–	–
Iron	7.85	7.39	1.29	–	–	–	–	–	–	–	–	100	–

the table. E_m is important mainly at low fluences near the threshold, and E_v dominates at higher fluences. As the fluence gets larger, neither of these energies has much influence, because they progressively become smaller and smaller parts of the total energy available for creating blowoff material as is evident in subsequent plots of impulses and coupling coefficients.

10. X-ray deposition code

The X-ray deposition code examines the target materials and input spectrum so that the numerical representation for the spectrum can be optimized for the discontinuities in the photoelectric absorption coefficients associated with the K- and L-absorption edges. The first output

from the code is the one-dimensional energy deposition profile in the target material. This is illustrated in Figure 15, which shows the profile for a copper-wire-array spectrum at a fluence of $\Phi_0 = 1.71 \, \text{kJ/cm}^2$ incident on Allende. As can be seen, the X-ray energy is deposited very near to the front surface, with a peak of $E \approx 2 \times 10^7$ J/g as its limiting value. This profile is then integrated over the material depth. Using the standard decomposition energies, the blowoff impulse, $I \approx 440$ Pa-s or 4.4×10^3 dyne $-$ s/cm^2. This leads to an impulse coupling coefficient, $C_M \approx 2.6 \times 10^{-5}$ s/m or 2.6 dyne-s/J. This process is repeated for various combinations of spectra and target materials being examined; the results are given in Table 6. This table also includes the impulses and coupling coefficients calculated using
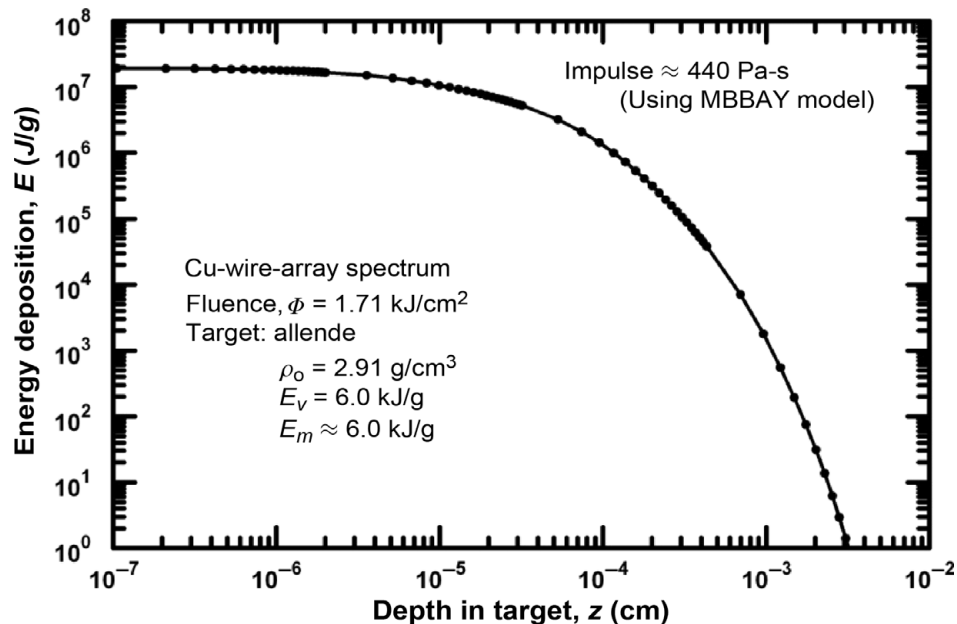

Figure 15. Energy deposition in Allende due to copper wire-array spectrum at a fluence of $\Phi_0 = 1.71 \, \text{kJ/cm}^2$. This calculation, generated by the X-ray code, is nearly flat in the region very near the front surface; the peak energy deposition at that surface is $E \approx 2 \times 10^4$ kJ/g. The flatness of the deposition profile shows that this is its limiting value, and that the spatial resolution used in the code is more than adequate. Using the data shown, the code also calculates the blowoff impulse according to the MBBAY model, as indicated on the plot. As with the previous figure, similar plots were generated for the various combinations of wire-array and target materials, as well as experimental fluence level. Calculations using the alternate values for E_v and E_m were also generated. The resultant values for all these calculated impulse values are listed in Table 6.
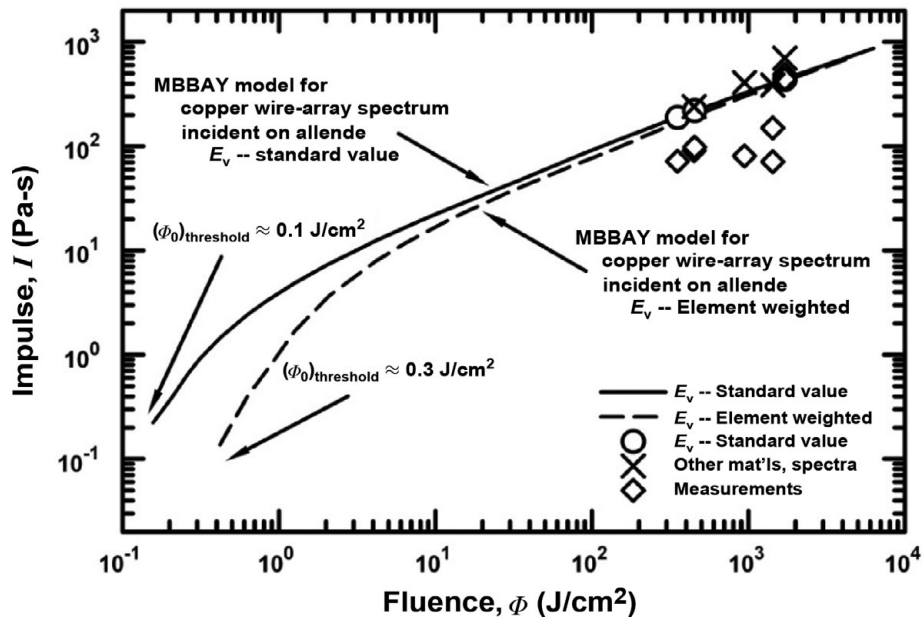
Figure 16. MBBAY model calculations for impulse versus fluence. These curves were generated for the X-ray spectrum from the Z-pinch copper wire array incident on Allende. The solid curve is for the standard decomposition energies and the dashed curve is for the alternate values. The circles and Xs represent calculations for the experimental conditions described in this paper; whereas the circles are for the cases represented by the curve, the Xs are for other spectra and materials. However, all the model calculations have very similar impulse/fluence curves because they are all at fluences well above the knee of the curve. For the standard decomposition energies, the model predicts that the threshold energy fluence for generating any blowoff impulse with the copper wire array and the Allende material is very low, at $(\Phi_0)_{\text{threshold}} \approx 0.1 \, \text{J/cm}^2$. Using the alternate decomposition energies this threshold is $(\Phi_0)_{\text{threshold}} \approx 0.3 \, \text{J/cm}^2$. For comparison, the diamonds show the experimental measurements, which are mostly well below the calculated results, typically by factors of 2 to 4. Note that 1 Pa-s = 10 "taps" = $10 \, \text{dyne} - \text{s/cm}^2$.

the alternate decomposition energies, as well as the relevant experimental impulse and coupling-coefficient data from Table 5. These latter coupling coefficients do not follow directly from the measured impulse and fluence because they were obtained using the impedance matching procedure described earlier.

Spectrum incidents on Allende, shown in Figure 16, were used for nearly half the shots considered in this section, so the full curves illustrating the model behavior are limited to this case. The solid curve uses the standard, generally accepted values for E_v and E_m, and the dashed curve employs weighted values based on elemental compositions of meteorite materials. Choices for E_v and E_m are important at low fluences than at high fluences. Similar calculations were performed for other combinations of X-ray spectrum, fluence, and target material, and the results are listed in Table 6. When impulse is plotted as a function of fluence, there is a threshold fluence below which blowoff impulse is not generated. In this case it is very low, at $(\Phi_0)_{\text{threshold}} \approx 0.1 \, \text{J/cm}^2$ for the solid curve and $(\Phi_0)_{\text{threshold}} \approx 0.3 \, \text{J/cm}^2$ for the dashed curve. Also, at fluences well above the knees of the curves, the curves coalesce and the impulse scales with the square root of the fluence. In addition to the model data for the three copper-wire-array shots and the Allende target material (circles), the figure includes the calculated impulse data for other shots

(Xs). For all the conditions examined here, the MBBAY model predicts very similar impulse behavior. The only possible exception is the aluminum sample exposed to the copper-wire-array spectrum because decomposition energies and absorption coefficients are substantially different from other materials examined and will have a higher impulse/fluence curve, with the impulse threshold shifted toward greater incident fluences, i.e. the entire curve will be shifted generally up and to the right. All the other calculated impulses fall very close to the curves as plotted.

When the same calculated data are used to plot the impulse coupling coefficients, as in Figure 17, a peak coupling or maximum efficiency occurs at an intermediate fluence that is roughly 10 times that of the impulse threshold (i.e. $\Phi_0 \approx 1 \, \text{kJ/cm}^2$ for the solid curve, and $\Phi_0 \approx 3 \, \text{kJ/cm}^2$ for the dashed curve). Both curves (solid for the standard decomposition energies, and dashed for the element-weighted values) were calculated for the copper-wire-array spectrum and the Allende target. As with the impulse, all the model data fall very close to the curve, with the exception of the one-outlier aluminum point. As before, this is due to its higher decomposition energies and other properties, which in turn shift the entire curve generally up and to the right. The existence of a peak impulse coupling coefficient has significant implications for optimizing application.
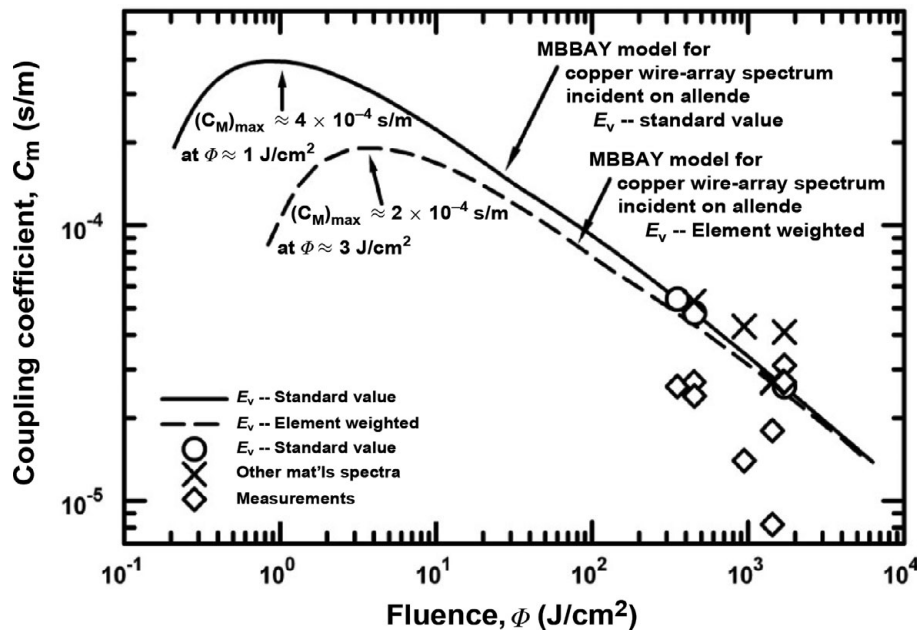
Figure 17. Impulse coupling coefficient as predicted by the MBBAY model for a copper-wire-array spectrum incident on Allende. The curves and the points are as in the previous figure. Note that the MBBAY model predicts a maximum coupling coefficient, C_M, at intermediate fluences. In this case $(C_M)_{max} \approx 4 \times 10^{-4}$ s/m for the standard Allende decomposition energies, and $(C_M)_{max} \approx 2 \times 10^{-4}$ s/m for alternate values. The fluences for the C_M peaks are a factor of 10 above the threshold fluences. As with the impulse, the experimentally measured coupling coefficients (diamonds) are mostly below the calculations by a factor of about two. Note that 1 s/m $= 10^5$ (dyne-s/cm^2)/(J/cm^2) $= 10^5$ dyne-s/J.

11. Impulse measurements

Both Figures 16 and 17 include the experimentally measured impulse and coupling coefficient data for these eight shots that mostly fall below model calculations and exhibit considerable scatter, although they do show the same general trends as the model results. The measured momenta are typically factors of two to four, and the coupling coefficients are up to a factor of two lower than model calculations. Some of the scatter in the data may be due to sample inhomogeneities or limitations in experimental reading times from finite lateral target dimensions. This might happen if the VISAR laser beam selectively measures response of either an inclusion or the matrix material, which would likely have a velocity history different from "homogenized" material, or it may be due to the influence of lateral wave reflections on the VISAR records. Window material helps to smooth out irregularities to some extent. Inhomogeneities also lead to variations in the blowoff process due to turbulent mixing at high fluences and decomposition energies at low fluences. Other phenomena such as "front-surface spall" or contributions from "non-blowoff impulse" (Appendix B) could lead to uncertainties in either model calculations or the experimental results. Errors in incident X-ray spectrum or fluence are not thought to be important because of their relative insensitivity of impulses and coupling coefficients at high fluences.

12. Discussion

It is important to distinguish between processes of momentum transfer (which involve material in and near the mean free path (MFP) for X-ray absorption) and downstream wave processing involving the entire sample). The momentum transfer process is affected by the X-ray cross-section of the target material (which determines the MFP), the total energy deposited in the MFP (which governs heating), and phase changes (which may also strongly affect material ejection). High-strength materials must absorb more energy to generate near-surface particulate ejecta and spall scabbing. By contrast, downstream waveform evolution does not affect the net momentum transfer. C_M is determined by near surface ejecta mechanisms operating during the initial X-ray interaction in the MFP.

Material EOSs are difficult to ascertain in an attenuating wave context such as in the present experiments. While some inferences can be made on the basis of wave transit times (corresponding to mean wave speeds), these experiments are not nearly as good for measuring EOSs as are (1) experiments with supported wave (i.e. non-attenuating), or (2) isentropic compression methods (Hall et al. 2001, 2002). Attenuation of an impulsive pressure wave depends on target material properties and affects Hugoniot states at different target locations. Hence, Hugoniot states reached at the rear surface are a function of initial impulse at the front surface and

waveform evolution during target transit. The wave carries a constant impulse until it interacts with target boundaries. The high-energy-density dynamic responses of natural-material targets depend on inhomogeneous meso- and macro-structures that give rise to turbulent mixing. Modeling this interactive behavior is analogous to predicting the outcome of a single pebble scattering off a collection of pebbles where a myriad of trajectories is sensitive to boundary conditions, shapes, and sizes that cannot all be considered fully. Such phenomenology is difficult to model in hydrocodes that idealize particle agglomerations as a homogeneous medium. Nonetheless, the normative results generated by this research are relevant to NEO hazard mitigation, astrophysics and planetary science, and modeling of weapon effects and energy coupling for nuclear tests, thereby assisting in nuclear test ban monitoring and compliance.

The present explicit modeling treatment, the MBBAY model, was developed using only basic hydrodynamics theory and conservation of energy and momentum, and should provide an estimate of the overall physical processes connected with the generation of radiation-induced blowoff impulse. That involves deposition of pulsed radiation energy into a target and the turbulent-free conversion of that energy into a dynamic impulse. As anticipated, experimental C_M values are generally lower than the model calculations. Individual contributing factors to these inconsistencies (e.g. decomposition energies and turbulence effects) have been discussed. From an experimental perspective the data reduction technique may have difficulties, possibly with regard to the impedance-matching approach that was employed. Front-surface spall and non-blowoff impulse may influence the measurements, and these are certainly not included explicitly in the present model calculations. Even larger sources of error are the material inhomogeneities, and the finite lateral dimensions of the samples; these are not in the calculations. Some of these effects may be treated explicitly in a complete time-dependent hydrodynamic analysis. If the input parameters are correct, the response phenomenology should also be correct, especially at high fluences where impulse increases slowly and is insensitive to most of the input details. On the other hand, inhomogeneities generate turbulence-mixing uncertainties that are difficult to quantify, and may be 10–100%.

Specifically, the measured C_M values range from approximately 25% to 100% of values from the BBAY calculations presented in Section 11. Some further comments about experimental errors are in order. The direct quantities used to calculate C_M from the experimental data are the time integral of the observed velocity history, the incident fluence, and the impedance correction. It is unlikely that the velocity history or the impedance correction is low by 2 to 4 times, or the fluence is high by 2 to 4 times. An impedance change in the path of a pressure wave may slightly increase the duration of the wave at that impedance discontinuity and tend to

increase the experimental C_M. Other important sources of error are likely to be due to turbulent mixing and the finite sample and window size. As mentioned above, integration of the velocity history must be truncated when the pressure wave has reached the back of the window and returned to the sample. Ironically, this is most likely to be a major factor for the Allende chondrite sample in shot Z1310, where experimental data appear to agree more closely with the MBBAY calculations.

Although momentum uptake for these materials uniformly occurred in a short time (∼5 ns), governed by incident pulse duration, mechanical wave dispersion varied greatly among samples. This dispersion caused slow loading (∼100 ns) observed in the inhomogeneous or porous samples in contrast with the sharp wavefronts observed for the aluminum samples and the relatively rapid loading (∼50 ns) for the iron and octahedrite samples. Combined with dispersive unloading, the truncation could seriously reduce the amount of the original pressure wave that actually contributes to the derived impulse. Thus, we must also consider physical errors that could affect the MBBAY calculations. The most important is likely to be the fluence to use for $\Phi_0^* = 1$. Inhomogeneities are also important factors for enhancing turbulence mixing and scatter.

13. Conclusions

Experiments using HED soft X-ray (∼10 A) irradiation on meteorite and planetary materials of astrophysical and geophysical interest indicate that consistent values can be obtained for impedance-corrected C_M. The reliability of EOS measurements depends on sample homogeneity, being greater for the low-porosity, kamacite-dominated metallic samples than for the more heterogeneous, stony meteorite materials. Materials analyzed include representative iron and stony meteorites, magnesium-rich olivine (solid and powder dunite), and Al and Fe calibration materials of approximate 1-mm thickness. Calculated front target surface radiation (plasma) pressures varied from 2.6 to 12.4 GPa. Based on computation, front surface (tenuous plasma) radiation C_M was approximately 0.6×10^{-5} s/m. Rear surface Hugoniot pressures varied from 5.3 and 10.6 GPa for Fe and Al calibration targets, 1.7 GPa for iron meteorites, 0.5–1.9 GPa for stony meteorites, 0.8 GPa for Si, 1.6–1.9 GPa for solid dunite, and 0.63 for powdered dunite. Calibration targets had much lower shock attenuation than inhomogeneous (stony) materials: 4.3–5.4 GPa/mm for Fe and 1.8 GPa/mm for Al. Attenuation varied from 7.9–9 GPa/mm in iron meteorites, 2–12 GPa/mm for stony meteorites, 6.1–5.8 GPa/mm for the solid dunite, and 7.1 GPa/mm for the powdered dunite.

Rear surface (mechanical)-corrected C_M based on momentum transfer varied from 1.9–3.1×10^{-5} s/m for stony meteorites, 2.67×10^{-5} for solid dunite, 0.49×10^{-5} for powdered dunite, 0.82–1.42×10^{-5} s/m for iron meteorites, and 1.8 and 2.7×10^{-5} s/m, respectively, for

Fe and Al calibration targets. These are consistent results with errors within the experimental measurement limitations on inhomogeneous materials used to model planetary interactions and NEO mitigation. Dunite powder had a reduced C_M due to the low rate of momentum transfer from the loose material. A significant fraction of the wave arrived late enough in time that it could not be reliably measured because of the finite size of the LiF window (see Section 7). There is an excellent agreement, $\sim$1%, in C_M values between the relatively homogeneous solid rock mesosiderite and equilibrated chondrite targets, but there is dispersion in C_M among the three unequilibrated CV3 target samples thought to be due to the different chondrule to matrix ratios that affect the amount of momentum coupling jetting on the irradiated front surface. Also, the location of the VISAR fiber optic probe will detect shock velocities ranging in value of $\sim$40% depending on where the probe is placed (Remo and Furnish 2008), i.e. whether it is sampling the more rigid chondrule phases or the more friable and looser matrix phases. In terms of mechanical interactions, solid dunite is similar to the mesosiderite and the equilibrated chondrite, while powdered dunite may be thought of as an extreme case of an unequilibrated chondrite. Our results are also in very close agreement with geometrically extrapolated results from recent (Omega) laser-driven hohlraum plasma implosion experiments.

A key fluence level is approximately 10 Φ_0, $\sim$10$\times$ the energy per area required to vaporize the target absorption depth. In this regime, $C_M \propto \Phi^{(1/2)}$. At lower fluences, errors in Φ_0 are due to material strength and phase change thermodynamics. At higher fluencies further increases in fluence are partitioned into additional kinetic energy T of the ejecta and turbulent mixing. Present studies are performed at $\Phi \approx 1000\,\Phi_0$ where ejection modeling is less susceptible to errors from material heterogeneities or Φ_0 than for the lower fluences used. It is thought that the majority of the discrepancies is due to finite sample and window size, ablation-driven turbulent mixing, and resulting limits on velocity integration time (requiring us to truncate an integration). Overall, the MBBAY calculations discussed did not include energy losses from residual solid particle ejecta and other target response mechanisms, thereby giving higher values of C_M. Taking these factors into consideration, the experimental values are consistent with the theoretical analysis and account for variances in the experimental values for $C_M(I)$ for the CV3 and octahedrite meteorites.

Theoretical results indicate an asymptotic slight (monotonic) decrease consistent with (5a) and (6); i.e. $C_M \propto I^{-1/8}$ after a maximum $C_M(I)$ is achieved as shown in Hammerling and Remo (1995). At lower intensities, phase transition energy of the ejected material dominates. As I increases, $C_M(I)$ also increases up to a maximum value. At higher intensities more radiation energy is partitioned into ejecta kinetic energy and

total momentum transfer increases more slowly. At very high intensities more energy is lost to re-radiation and related effects, and $C_M(I)$ decreases slowly, but total (net) momentum transfer continues to increase (Lawrence et al. 2012) with $C_M \propto I^{-1/8}$ and specific impulse (momentum/area) $\propto F_{Rad}^{1/2}$. The $C_M(I)$ for targets below or above the range of experimental values considered here and the MBBAY results agree within less than a factor of 2 in variation except for the two (heterogeneous) octahedrite meteorites. Similar dichotomies appear for the CV3 and octahedrite meteorites that can be resolved with additional experiments at higher and lower intensities for different targets.

14. Future research

Future experiments aspiring to characterize the response of inhomogeneous materials to HED soft X-rays should use spatially resolved diagnostics such as the line-imaging VISAR to allow more precise conclusions to be drawn on distinct material response to the X-ray flux. This can be achieved by using multipoint or line-imaging diagnostics. Alternatively, wave-averaging methods, such as a thin Al or Fe buffer, could be used; however, this is less desirable due to small sizes of samples and windows.

Sample recovery would allow post-irradiation chemical and texture analysis on target microstructures to study phase transformation, zone melting, hydrodynamics, and turbulent-mixing-driven species migration. For example, similar experiments could be performed on thicker solid and powder dunite and stony meteorites and dunite/iron powders. These experiments could use a fast electric shutter to seal off the target from the plasma pinch debris, ensuring that signatures of the debris do not confuse the post-shot analysis.

It would be worthwhile to separate the effects of line emissions and thermal radiation (perhaps through the use of thin Kapton windows). The deposition depths differ significantly for these two types of radiation, and consequently, the coupling physics differs as well. To further explore the enhanced momentum coupling and C_M associated with finely powdered materials, additional experiments on lunar soil simulants, powdered Fe, and powdered dunite should be carried out with the intention of sample recovery.

Appendix A. Detailed petrographic descriptions of samples

Fe–Ni meteorites

The Fe–Ni (Odessa) iron meteorite samples used in these experiments are prepared from a fragment from an impact $\sim$50,000 years ago (the late Pleistocene) in Odessa, Texas. It is a typical coarse octahedrite (Og). The primary mineral phases are Fe–Ni alloys, Ni-depleted bcc-phase kamacite (90%), and Ni-rich fcc phases, taenite, and plessite. Other common minerals are schriebersite $((FeNi)_3P)$, troilite (iron sulfite) nodules mixed with graphite, graphite nodules, and cohenite (iron carbide). Acoustic P and S wave velocity profiles for Odessa indicate wave propagation speeds corresponding to different material phases.[2] The Fe–Ni meteorite Hugoniot response is dominated by a single crystal kamacite phase with bulk octahedral properties. Mechanical impacts over a stress range of 2–20 GPa indicate loading strength, α to ε transition signatures similar to Armco iron, and no evidence for ductile to brittle transition at extremely high loading rates (Furnish et al. 1994, 1995). Under Z-pinch X-radiation, Fe–Ni meteorites yielded relations between PH (Hugoniot pressure) versus u_p (particle velocity) and u_s (wave speed) versus u_p as shown in Table 4 and Figures 3 and 4. These values agree with those of the Hugoniot states for the Henbury medium Octahedrite (Furnish et al. 1994, 1995). The Odessa coarse octahedrites irradiated in the Z-pinch experiments had lower stress levels than did the Armco iron values due to mineral inclusions. Fe and Al calibration samples yielded consistent results compared with mechanical impact (Meyer 1994) and had much lower pressure gradients, 9.5 to $\sim$5.3 GPa for Fe and 12.4 to 10.6 GPa for Al over a 1-mm travel distance, than did Fe meteorites.

Stony meteorites

Tests were conducted with three stony meteorites: CV3 (Allende) chondrite, (Vacamuerta) mesosiderite, and (Tuxtuac) LL6 refractory chondrite. The CV3 sample was loose and friable, by contrast with the stronger (metamorphosed) LL6 refractory chondrite and mesosiderite. Their mineralogy is as follows (Remo 1999):

1. The CV3 has a density of 2.91 g/cm^3 and is composed of large chondrules surrounded by lighter and darker matrices. The former matrix appears to be magnesium-rich olivine, while the latter appears to be composed of calcium-rich clino-pyroxene (Ca[Fe,Mg]2Si2O6) quenched from a melt with phenocrysts of olivine ($[Fe_{\sim 0.1}Mg_{0.9}]_2SiO_4$ in equilibrium. Fe–Ni, pyrite, troilite, and pyrrhotite were also observed.

2. The mesosiderite, with a density of 3.6 g/cm^3, is a fine-grained and irregular highly altered material via brecciation, and recrystallization is composed primarily of calcium feldspar anorthite ($CaAl_2Si_2O_8$), but also appears to contain apatite (Ca_3PO_4), pyroxene, chromite, fine-grained Fe–Ni, troilite, and pyrrhotite. By contrast with the refractory chondrite, it is non-magnetic.

3. The refractory chondrite, with a density of 3.02 g/cm^3, is a low metal chondrite with calcium-rich clinopyroxene refractory crystals and olivine phases with pyroxene in exosolution, and feldspar.

The friability of the CV3 sample may have enhanced front surface jetting, affecting momentum transfer. Primitive CV3 meteorites also have steep, energy-absorbing pressure gradients, while the (stronger) metamorphosed targets have smaller pressure gradients. These materials and most natural terrestrial minerals are dominated by pores and grain boundaries that scatter shock wavefronts differently for each specimen, affecting the observed waveforms. The velocimetry diagnostic method used (point VISAR) unfortunately does not give information about the point-to-point variation in velocity history, or about where in that variation the observed point lies. The line-imaging VISAR may obviate this difficulty. In some cases such as when many different phases and/or inhomogeneities are present, it may be preferable to use simple rear surface (mechanical) gross displacement measurements (Remo and Adams 2008).

Dunite

Dunite is a dense polycrystalline igneous (plutonic) rock comprising mainly olivine, a magnesium silicate. The present samples, from Almklovdalen, Norway, consist of >90% typically large (0.1 to 0.5 mm) olivine grains of forsterite composition (Fo 93.1+/−0.5, NiO $\sim$0.4 wt.%), some large (0.1 to 0.5 mm) chlorite grains (a few percent), rare (<1%) grains of orthopyroxene (50 μm), and chromite (<10 μm), chemically and mechanically consistent except for occasional inhomogeneities. The dunite powder mostly consisted of relatively large olivine (50–300 μm) and a few percent large (100–300 μm) chlorite crystals derived from the same mineral source. This material was used both with an initial density of 3.30 g/cm^3 and in powdered and compressed form at a density 2.78 g/cm^3 with 20% porosity and a size range of 5–300 μm.

Appendix 2. Brief explanation of front-surface spall and non-blowoff momentum

"Front-surface spall" and "non-blowoff momentum" may be unfamiliar terms. When a very short-duration (relative to material shock response) pulsed radiation load deposits its energy in a solid target, the resultant energy deposition profile is usually a decreasing exponential with target depth. If the intensity is sufficient to vaporize the front surface, then that surface will be explosively blown off. In the remaining target material a compression wave will propagate in the downstream direction. Typically it will have a ramp loading, evolving into a shock wave, followed by a slow fall-off to a near-zero value. If the longitudinal stress of the wave profile is integrated with time at a specific position, the resultant value will be a momentum that is related to the "blowoff impulse" generated by the vaporized material. Now consider the case where the instantaneous exponential energy deposition profile is insufficient to vaporize the front surface. This could occur due to a low fluence, or a material absorption coefficient that spreads the exponential deposition profile over a much greater distance. A pressure or shock wave will still be generated due to thermal heating and expansion, and its integral will also yield a momentum. However, this momentum cannot be related to the blowoff impulse, because there is none. Its pressure profile will be somewhat analogous to a shock wave incident on a free surface, where a "phase reversal" in pressure occurs. That is, it will consist of a compressive portion followed by a mirror-like tensile portion. If the tensile amplitude is large enough, the front surface could fracture in a fashion similar to the classic rear-surface spall. This is the origin of "front-surface spall." The result of this is that any pressure-history integration to measure impulse must be examined carefully to ensure that reasonable account is taken for both blowoff and non-blowoff portions of the momentum. Most situations will consist of a mixture of the above two cases. However, in the limiting conditions of very high or very low energy fluences, one or the other of the above two situations may be safely neglected.

References

Atzeni, S. and Meyer-ter-Vehn, J. 2004 *The Physics of Inertial Fusion.* Oxford, UK: Clarendon Press.

Dolan, D. H. 2006 *Foundations of VISAR Analysis.* Report SAND2006-1950, Sandia National Laboratories, Albuquerque, NM, 54 pp.

Furnish, M. D., Boslough, M. B., Gray, G. T. III and Remo, J. L. 1995 Dynamic properties measurement for asteroids, comets, and meteorite material applicable to impact modeling and mitigation calculations. *Int. J. Impact Eng.* **17**, 341–352.

Furnish, M. D., Gray, G. T. III and Remo, J. L. 1994 Dynamical behavior of octahedrite from the Henbury meteorite. In: *High Pressure Science and Technology* (eds. S. C. Schmidt, J. W. Shaner, G. A. Samara and M. Ross). New York: AIP Press, pp. 819–822.

Hall, C. A., Asay, J. R., Knudson, M. D., Hayes, D. B., Lemke, R. L., Davis, J.- P. and Deeney, C. 2002 Recent advances in quasi-isentropic compression experiments (ICE) on the Sandia Z accelerator. In: *Shock Compression of Condensed Matter – 2001* (eds. M. D. Furnish, N. N. Thadhani and Y. Horie). New York: AIP Press, pp. 1163–1168.

Hall, C. A., Asay, J. R., Knudson, M. D., Stygar, W. A., Speilman, R. B., Pointon, T. D., Reisman, D. R., Toor, A. and Cauble, R. C. 2001 Experimental configuration for isentropic compression of solids using pulsed magnetic loading. *Rev. Sci. Instr.* **72**, 3587–3595.

Hammerling, P. and Remo, J. L. 1995 NEO interaction with nuclear radiation. *Acta Astronaut.* **36**, 337–346.

Hertel, E. S. Jr., Bell, R. L., Elrick, M. G., Farnsworth, A. V., Kerley, G. I., McGlaun, J. M., Petney, S. V., Silling, S. A., Taylor, P. A. and Yarrington, L. 1993 CTH: a software family for multi-dimensional shock physics analysis. In: *Proceedings of the 19th International Symposium on Shock Waves*, Marseilles, France, pp. 377–382.

Hicks, D. G., Spears, B. K., Braun, D. G., Olson, R. E., Sorce, C. M., Celliers, P. M., Collins, G. W. and Landen, O. L. 2010 Convergent ablator performance measurements. *Phys. Plasmas* **17**, 102703.

Lawrence, R. J. 1992 The Equivalence of simple models for radiation-induced impulse. In: *Shock Compression of Condensed Matter – 1991* (eds. S. C. Schmidt, R. J. Dick, D. G. Tasker and J. W. Forbes). Amsterdam, Netherlands: Elsevier Science, pp. 757–788.

Lawrence, R. J., Furnish, M. D. and Remo, J. L. 2012 Analytic models for pulsed x-ray impulsive coupling. In: *Shock Compression of Condensed Matter – Proceedings of the Conference of the American Physical Society Topical Group on Shock Compression of Condensed Matter 2011* (eds. M. L. Elert, W. T. Buttler, J. P. Borg, J. L. Jordan and T. J. Vogler), AIP Conference Proceedings, vol. 1426. New York: AIP Press, pp. 883–886.

Lindl, J. 1995 Development of the indirect-drive approach to inertial confinement fusion and the target physics basis for ignition and gain. *Phys. Plasmas* **2**, 3933.

Lowen, R., Schaibly, J. and Stephens, T. 1993 *X-ray Radiation Transport Program (User's Handbook)*. San Diego, CA: Horizons Technology (DNA-EH92-012-G-V1 (HTI-SDR-92–051), Defense Nuclear Agency, Alexandria, VA).

McQueen, R. G., Marsh, S. P., Taylor, J. W., Fritz, J. N. and Carter, W. J. 1970 The equation of state of solids from shock wave studies. In: *High-Velocity Impact Phenomena* (ed. R. Kinslow). Middlesex, MA: Academic Press, pp. 293–417.

Meyer, M. A. 1994 *Dynamic Behavior of Materials.* New York: Wiley.

Newlander, C. D., Place, J. R., Scammon, R. J. and Copus, E. R. 1978 *Nuclear Hardness Evaluation Procedures (NHEP) Program, Phase 1: Analytic Technique Survey*. Report no. AFWL-TR-78-18, Air Force Weapons Laboratory, Kirtland AFB, NM.

Remo, J. L. 1999 High-power-pulsed 1054-nm laser induced shock pressure and momentum, and energy coupling to iron-nickel and stony meteorites. *Laser Part. Beams* **17**, 25–44.

Remo, J. L. and Adams, R. G. 2008 High-energy density laser interactions with planetary and astrophysical materials: methodology and data. *Proc. SPIE Int. Soc. Opt. Eng.* **7005**, 70052M-1-11.

Remo, J. L. and Furnish, M. D. 2002 High intensity x-ray coupling to meteorite targets. In: *Shock Compression of Condensed Matter – 2001* (eds. M. D. Furnish, N. N. Thadhani and Y. Horie) New York: AIP Press, pp. 1163–1168.

Remo, J. L. and Furnish, M. D. 2008 Analysis of Z-pinch shock wave experiments on meteorites and planetary materials. *Int. J. Impact Eng.* **35**, 1516–1521.

Remo, J. L., Furnish, M. D. and Lawrence, R. J. 2012 Soft x-ray shock loading and momentum coupling in meteorite and planetary materials. In: *The Proceedings of the 17th Biennial International Conference of the APS Topical Group on Shock Compression of Condensed Matter 2011* (ed. M. L. Elert, W. T. Buttler, J. P. Borg, J. L. Jordan and T. J. Vogler). New York: AIP Press, pp. 883–886.

Remo, J. L., Petaev, M. I. and Jacobsen, S. B. 2008 Experimental simulation of high P-T planetary processes: physics of laser-induced shocks in solid and powdered targets. *Lunar Planet. Sci.* **39**, 1420.

Shafer, B. P., Garcia, M. D., Managan, R. A., Remo, J. L., Rosenkilde, C. E., Scammon, R. J., Snell, C. M. and Stellingwerf, R. F. 1994 The coupling of energy to asteroids and comets. In: *Hazards Due to Comets and Asteroids* (ed. T. Gehrels) Tucson AZ: University of Arizona Press, pp. 955–1012.

Shafer, B. P., Garcia, M. D., Managan, R. A., Remo, J. L., Rosenkilde, C. E., Scammon, R. J., Snell, C. M. and Stellingwerf, R. F. 1997 Momentum coupling to NEOs. In *Near-Earth Objects: The United Nations International Conference* (Annals of the New York Academy of Science, vol. 822) (ed. J. L. Remo). New York: New York Academy of Science, pp. 552–565.